


RESEARCH ARTICLE OPEN ACCESS

Cut Finite Element 3D Acoustic Shape Optimization of a Compression Driver Taking Viscothermal Losses Into Account

Martin Berggren¹  | Anders Bernland¹ | André Massing² | Daniel Noreland³ | Eddie Wadbro⁴

¹Department of Computing Science, Umeå University, Umeå, Sweden | ²Department of Mathematical Sciences, Norwegian University of Science and Technology, Trondheim, Norway | ³The Forestry Research Institute of Sweden, Uppsala, Sweden | ⁴Department of Mathematics and Computer Science, Karlstad University, Karlstad, Sweden

Correspondence: Martin Berggren (martin.berggren@cs.umu.se)

Received: 7 April 2025 | **Revised:** 15 December 2025 | **Accepted:** 30 January 2026

Keywords: compression driver | cut finite element method | phase plug | shape calculus | shape optimization | viscothermal acoustics

ABSTRACT

Wave propagation effects such as resonance and interference effects complicate the design of many acoustic devices, particularly when the dimensions of the device are in the order of the operating wavelength. At the same time, these complications also offer an opportunity for numerical optimization schemes to outperform designs achieved using traditional methodology. An example of a device sensitive to resonance and interference effects is the *compression driver*, the standard sound source for midrange acoustic horns in public address systems. Although ingenious and rather simple design guidelines have been developed, these unfortunately only apply to particular conceptual compression driver layouts. Here, we address a configuration for which no simple rules exist and apply numerical shape optimization for the design task. We employ a level-set geometry description of the crucial part of the compression driver interior. To avoid mesh changes when the level-set function is updated by a gradient-based optimization algorithm, we rely on the cut finite element (CutFEM) technique for the acoustic modeling. A particular modeling challenge here is that viscothermal losses cannot be ignored, due to narrow chambers and slits in the device. Up to quite recently, the modeling of such losses has required computationally expensive solutions of the linearized, compressible Navier–Stokes equations, making the use of shape optimization extremely challenging. Fortunately, a recently developed, accurate, but computationally inexpensive boundary-layer model is applicable in this case. For the first time in the context of a CutFEM/level-set method, the shape calculus needed to compute derivatives for the optimization algorithm is carried out in the fully discrete case, taking into account the discontinuities along the design boundary of the pressure derivatives and the normal field. Applying these techniques, the algorithm was able to successfully design the interior of a compression driver so that the final frequency response very closely matches an ideal response, derived by a lumped circuit model where wave interference effects are not accounted for.

This is an open access article under the terms of the [Creative Commons Attribution](https://creativecommons.org/licenses/by/4.0/) License, which permits use, distribution and reproduction in any medium, provided the original work is properly cited.

© 2026 The Author(s). *International Journal for Numerical Methods in Engineering* published by John Wiley & Sons Ltd.

1 | Introduction

We present a case study in computational design optimization that aims to demonstrate how recent progress, both in mathematical modeling and design optimization techniques, may potentially revive a design concept rarely used due to difficulties in providing simple, explicit design guidelines. The modeling progress concerns acoustic viscothermal (also called thermoviscous) losses, and the improved design optimization technique involves a novel shape calculus approach for CutFEM discretizations in combination with level-set geometry descriptions. The target application we consider is the *compression driver*, a standard sound source for the acoustic horns that are used in public address systems aimed at large auditoria and outdoors. In particular, we will optimize the device in the rarely-used *radial* orientation of the so-called phase plugs. We will now shortly introduce these improved techniques, introduce the device under consideration, and outline the content of the rest of the contribution.

1.1 | Viscothermal Design Optimization

The mathematical modeling of viscothermal losses is of importance for acoustic devices in which the acoustic waves interact with large areas of solid surfaces, for instance, in waveguides, acoustic liners, and geometrically narrow devices. One example of a narrow device is the compression driver considered here; other examples are miniaturized devices such as headphones, microphones, mobile phones, and hearing aids.

It is only recently that numerical optimization of acoustic devices has been carried out using methods that can account for viscothermal losses. To a high computational cost, particularly for the three-dimensional cases we consider here, such losses can within the linear regime be accurately modeled using the linearized, compressible Navier–Stokes equations. In addition to the cost, a problematic issue of using these equations in the context of design optimization is the extreme scale separation between the viscothermal and wave propagation effects. The viscothermal losses are typically concentrated in exceedingly thin boundary layers close to solid walls. For instance, for air in the audio regime 20 Hz–20 kHz, the thickness of these boundary layers is smaller than the wavelength by a factor of 10^{-5} – 10^{-3} [1]. Thus, to achieve reasonable computing times, it is necessary to employ aggressive mesh refinement strategies along solid boundaries, preferably in the form of highly anisotropic meshes, thin in the wall-normal direction and stretched-out in the tangential direction, due to the scale separation between wall-normal and tangential directions ([1], Appendix A). The management of such meshes in a shape-optimization context is challenging.

However, the scale separation between wave and viscothermal effects can also be exploited to arrive at a simplified model of lower computational cost. Such a model, the sequential linear Navier–Stokes model, was developed by Kampinga [2]. As for the full Navier–Stokes equations, this simplified model unfortunately still requires accurate spatial resolution of the boundary layers and thus aggressive mesh refinements. Noguchi & Yamada [3] use the Kampinga model to optimize a sound-absorbing pipe in 2D axial symmetry, employing isotropic mesh refinements based on approximate computations of the signed distance function. The design sensitivity analysis utilized the adjoint-equation approach; however, the contributions from the viscothermal terms in the final gradient expressions were ignored in the optimization algorithm.

One way to circumvent the need for resolution of the boundary layers is to use a boundary-element formulation, which does not require a mesh inside the domain. Such an approach was used by Andersen, Henriquez, and Aage [4, 5] to optimize the shape of quarter-wave and Helmholtz resonators in 2D axial symmetry. Their viscothermal model is similar to the Kampinga model, but the resulting Helmholtz and diffusion equations are solved using boundary-element techniques. Although the use of the boundary-element method reduces the spatial dimensionality by 1 and circumvents the need for volume meshes, the computational cost for solving the system of equations appears to be somewhat high. However, Preuss et al. [6] have carried out initial studies aiming to reduce the computational cost and improve the conditioning of the resulting linear system.

The low reduced frequency model [7] is an even simpler and faster viscothermal model that can be used for special geometries, such as narrow slits and tubes. Christensen [8] used such a model for material-distribution topology optimization, where the cross-section shape of a narrow pipe was designed to maximize the viscous losses.

A completely different class of viscothermal models is based on boundary-layer theory, such as the model devised by three of the authors to the current contribution [1]. This model uses the standard, isentropic Helmholtz equation in the interior of the domain and models the viscothermal losses through a generalized impedance (a so-called Wentzell) boundary

condition on solid boundaries. The computational cost is essentially the same as for lossless acoustics, and the accuracy is comparable with the full linearized Navier–Stokes equation as long as boundary layers from opposing walls do not overlap and as long as the wall curvatures are not too extreme. In fact, the model seems to work surprisingly well even at really small scales, such as in the modeling of porous materials [9]. This viscothermal model has been used for design optimization only a few times so far, and only in 2D. The model was used by Tissot, Billard, and Garbard [10] to optimize for maximum absorption the interior shape of a Helmholtz resonator, thought of as an element to be periodically repeated to form an acoustic liner. Similarly to what we do here, the geometry was specified using a level-set function, and a CutFEM approach was used for discretization, whereas, in contrast to our approach, a fully discrete shape calculus was not attempted in their contribution. Dilgen, Aage, and Jensen [11] considered topology optimization of a hearing instrument, utilizing a vibroacoustic model for which the viscothermal losses were modeled using the boundary-condition approach. They also employed a level-set-function geometry description in combination with a CutFEM discretization approach. Parts of the calculations involved in the sensitivity analysis were carried out approximately using finite differences. Recently, Mousavi et al. [12, 13] introduced the boundary-layer model in a completely different optimization scenario, using so-called material-distribution (or density-based) topology optimization. In this scenario, the geometry is represented as a varying density-like coefficient in the governing equations. Such methods can produce designs with arbitrary topological complexity at the price of producing stair-cased boundaries and needing very fine meshes to accurately approximate curved boundaries.

1.2 | The Target Application

The most common sound source used in loudspeakers is the moving-coil dynamic transducer. When the diaphragm of such a driver is oscillating in free air, only a small fraction of its vibrational energy is converted to propagating sound waves due to the mismatch of acoustic impedance between air and the solid material in the diaphragm. Already in the 1920s, Hanna & Slepian [14] realized that better impedance matching could be achieved by placing the diaphragm in a cylindrical compression chamber with a narrow outlet attached to the throat of an acoustic horn. It was soon realized that the way in which the outlet from the compression driver is connected to the horn throat is important for acoustic performance; this part of the device is now known as the *phase plug*. The electrodynamic motor, the compression chamber, and the phase plug are typically mounted together to form a *compression driver*, which to this day is universally used to feed acoustic horns at mid to high frequencies in public address systems. The book by Kolbrek and Dunker [15] contains a recent and extremely comprehensive discussion on the history as well as theory of acoustic horns and drivers.

A main challenge in the design of the compression driver is to avoid resonance and interference phenomena, as they cause an uneven frequency response and may aggravate nonlinearities. A first issue is radial modes appearing in the compression chamber. In most commercially available devices, the compression chamber contains several outlets oriented in the annular direction, relying on the ingenious design rules first introduced by Smith [16]. Using such *Smith slits*, that is, placing N circumferential channels following the guidelines, N radial modes in the compression chamber can be suppressed. Dodd and Oclée-Brown [17, 18] modified Smith's guidelines to curved and Voishvillo [19] to ring-shaped diaphragms.

However, the phase plug that connects the slits to the horn throat can create additional resonances through wave interference between the channels. A reasonable guideline for the design of the channels in the phase plug is that these should be of equal path length. However, this requirement still does not prevent internal resonances from occurring. Bezzola [20] briefly reported results of optimizing the channels using the commercial Comsol Multiphysics software (likely using the lossless Helmholtz equation). In a previous contribution, three of the authors of the current article applied numerical shape optimization to the design of the channels in the phase plug of a compression driver equipped with Smith slits [21]. We concluded that the shape-optimized channels indeed improved the frequency response compared to the initial straight-channel design, but that multiple resonances unfortunately also remained in the optimized device. Another conclusion from the study was that viscothermal boundary-layer losses are quite prominent, due to the wave propagation being confined in a very narrow geometry. To lower the complexity and computational cost of the calculations, we carried out the optimization neglecting these losses, but evaluated the performance on the final geometry accounting for the viscothermal losses. However, thanks to modeling advances [1], we will here be able to include the modeling of the losses also in the optimization step.

Here we will consider the case when the outlets from the compression chamber are oriented in the *radial* direction. This design choice is rare in commercial units, and only little analysis has been carried out. The most complete discussion is

likely the chapter on radial outlets in the thesis of Oclee-Brown [18]. To fit typical geometries found in compression drivers, Oclee-Brown studies the wave propagation in the compression chamber by expanding the solution to the Helmholtz equation for the acoustic pressure in spherical coordinates. The analysis suggests that the number of outlets should be large enough to suppress circumferential modes in the chamber, and that radial modes can be suppressed by a slight modification of constant annular-width channel outlets.

Concerning the design of a phase plug that connects radially-oriented outlets into a waveguide to be fed into a horn, there seem to be no guidelines at all based on acoustic analysis in the literature. Here we will utilize gradient-based shape optimization for this task, based on a further development of the method we used for designing phase plugs for circumferential Smith slits [21]. The method relies on a level-set description of the geometry, which allows complex shapes to be treated in the optimization. In previous projects, the use of a level-set description has allowed unexpected and non-trivial shapes to appear in acoustic shape optimization studies [21, 22]. We combine the level-set geometry description with a fictitious-domain method known as CutFEM [23]. That is, the boundary of the computational domain, here the phase-plug wall, is allowed to migrate arbitrarily through a fixed computational mesh, which means that only partial contributions to the governing equations come from the finite-element mesh elements that are intersected by the boundary. Moreover, boundary conditions for the walls of the phase plug have to be assigned to the boundary surfaces that cut through the elements. As opposed to the previous study [21], the calculations need to be carried out here in three space dimensions. Previously, CutFEM/XFEM approaches have successfully been used for the shape optimization of, for instance, elastic structures [24–26], vibroacoustic problems [27–29], and flow patterns [30, 31].

1.3 | Overview and Novelties of the Article

In Section 2 and Appendix A, we review the acoustic mechanism of the compression driver and derive an expression that specifies the performance under idealized conditions, an expression that will be used in our most successful optimization formulation. Modeling details, the optimization formulation, and details of the discretization for our target application are introduced in Sections 4–6. A major difference with the previous study [21] is that we here will consider viscothermal losses also during the optimization, based on the model discussed above [1]. The viscothermal boundary condition needs to be supplied to the walls of the phase plug, subject to design, which significantly complicates the shape calculus. For the first time, to the best of our knowledge, this calculus will be carried out in the fully discrete case, taking into account that the derivatives of the acoustic pressure as well as the normal field of the boundary are, in general, discontinuous between elements. For this calculus, we will rely on formulas proven in a recent publication [32]. The calculus is detailed in Appendix B, and the formulas are summarized in Section 7. We present the results of the phase plug optimization in Section 8, results which seem to indicate surprisingly favorable acoustic properties of properly shaped radially-oriented phase plugs, as discussed in the concluding Section 9. Note that radially-oriented outlets of phase plugs are rare in commercially available devices, likely due to a lack of design guidelines. Hence, the present optimization study, the first of its kind, may serve as a motivation to further investigate this alternative design concept.

Remark 1.1. After submission of the current manuscript, the correctness of the underlying formulas [32], as well as extensions of them, was verified by Automatic Differentiation (AD) in an article by Wegert et al. [33]. We further discuss the use of AD in Remark 7.3 below.

2 | The Compression Driver Mechanism

To recognize the issues faced when designing a compression drive phase plug, it is necessary first to appreciate the fundamental mechanism of the compression driver. In any loudspeaker transducer, a vibrating diaphragm induces the acoustic waves that will be transmitted to the surroundings. The basic function of the compression driver is to generate a high sound pressure level while only requiring a small displacement of the diaphragm. Hanna and Slepian [14] are generally recognized to be the first in 1924 to describe and analyze such a device.

Under a number of strong assumptions, it is possible to devise a lumped-parameter model for the acoustic pressure generated by the movement of a diaphragm in a model compression driver. We will see that only two geometric properties of the device, its compression ratio and the depth of the compression chamber, govern its performance under these assumptions. These two quantities constitute the fundamental parameters to be chosen by the designer.

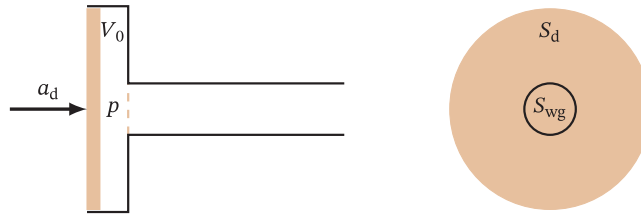


FIGURE 1 | A conceptual cylindrical compression driver. Cross-section view through axis (left) and orthogonal to axis (right).

Consider the simplified model of a compression driver illustrated in Figure 1. A diaphragm of cross-sectional area S_d is positioned in a cylindrical chamber with rest volume V_0 and with an outlet attached to a waveguide with cross-sectional area S_{wg} . We make the following idealized assumptions.

Assumptions 2.1.

- i. The diaphragm moves axially as a solid piston given a time-harmonic movement with acceleration amplitude a_d .
- ii. The pressure is the same at each point within the compression chamber.
- iii. The compression within the chamber is isentropic, and the air is an ideal gas.
- iv. Linearity of the acoustic quantities.
- v. The waveguide is perfectly terminated; that is, the waves traveling to the right in the waveguide will be perfectly absorbed.

Due to the time-harmonic assumption, the acoustic pressure in the compression chamber and the acceleration of the diaphragm, as a function of time, can be written

$$P(t) = \text{Re}(p e^{i\omega t}), \quad A_d(t) = \text{Re}(a_d e^{i\omega t}), \quad (1)$$

where ω is the angular frequency of the movement and p and a_d are complex amplitudes. Under Assumptions 2.1, it can be shown that the acoustic pressure and diaphragm acceleration amplitudes are related through the equation

$$k\left(-dk + \frac{i}{\kappa}\right)p = \rho_0 a_d. \quad (2)$$

The geometric parameters of formula (2) are

$$d = \frac{V_0}{S_d}, \quad \kappa = \frac{S_d}{S_{wg}}, \quad (3)$$

that is, the compression chamber depth d in the simple geometry of Figure 1 and the compression ratio κ . Moreover, ρ_0 is the static density of air and $k = \omega/c_0$ the wave number, in which c_0 is the speed of sound.

Formula (2) is likely no surprise for the acoustician and could be extracted, for instance, from the much more comprehensive lumped-parameter performance analysis found in Kolbrek & Dunker's monograph ([15], section 18.4.4). However, the precise formulation given above will be useful in the following, and we are not aware of any source containing this exact formula, which is why we provide a short derivation in Appendix A.

To appreciate the effects of the compression chamber on the frequency response, we will consider the pressure amplitude, which by expression (2) will be

$$|p| = \frac{\rho_0 |a_d|}{k(d^2 k^2 + 1/\kappa^2)^{1/2}}. \quad (4)$$

Figure 2 shows the frequency response of the pressure amplitude, according to formula (4) with constant $|a_d|$, for a variety of compression ratios and chamber depths. We note that an increased compression ratio has a dramatically positive effect on the delivered sound pressure level, and that an increase in compression ratio should be accompanied by a narrowing of the chamber depth in order not to worsen the dropoff for higher frequencies.

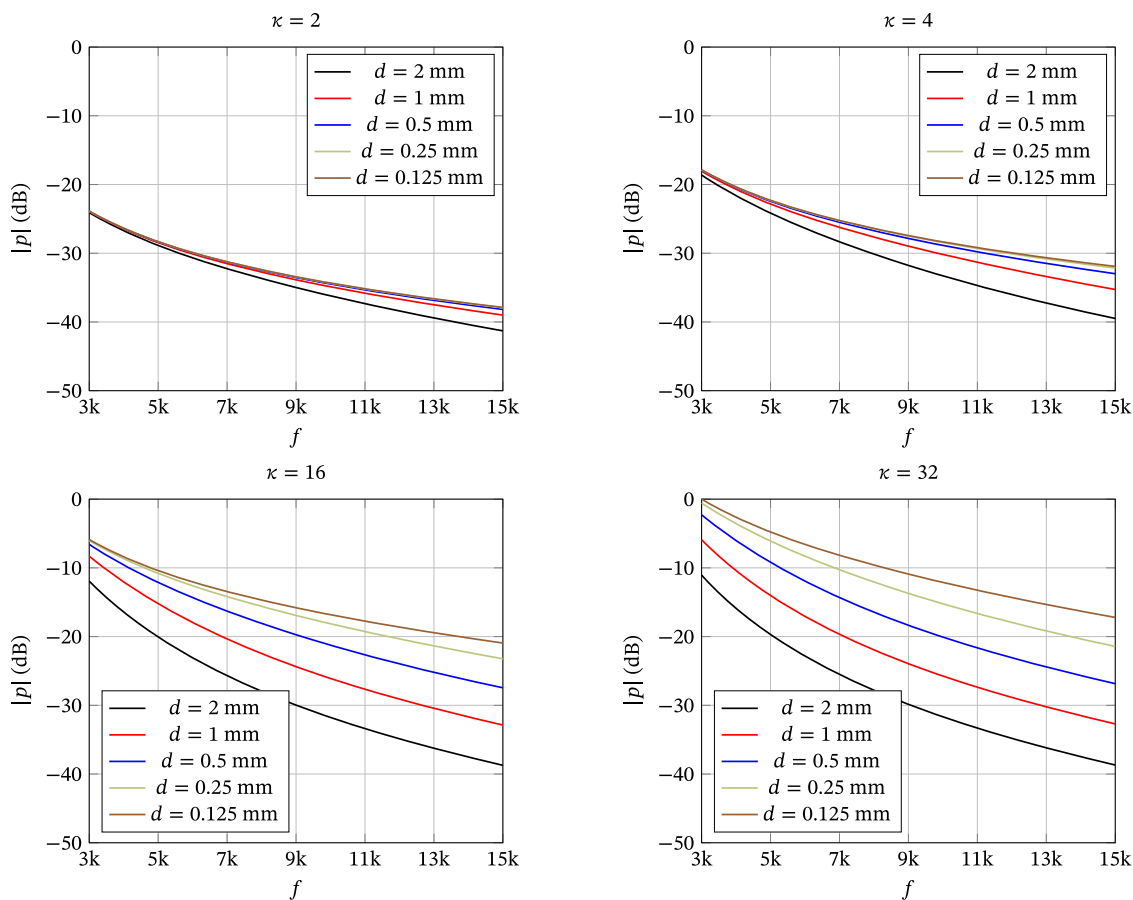


FIGURE 2 | The frequency response, given a fixed diaphragm acceleration, of the lumped model for various compression ratios $[\kappa]$ and chamber depths $[d]$. (Plots scaled by the maximum sound pressure of all graphs.)

Remark 2.2. Note that no real compression driver unit will possess a frequency response like the ones in Figure 2, since the diaphragm acceleration cannot be expected to be constant throughout the frequency range. Typically, a moving-coil dynamic transducer supplies the diaphragm motion, and the frequency response will then depend on the electrical and mechanical properties of the transducer and how they interact with the compression chamber. The reason for providing the curves in Figure 2 is to clarify the effects of the compression driver geometry; to obtain the actual frequency response of the system, a complete, coupled model is needed that also includes the transducer and a more realistic model for the waveguide load to replace Assumption 2.1v.

3 | Violations of Assumption 2.1

In real compression drivers, Assumptions 2.1 will be violated to various degrees. The sound pressure level in the chamber can be very high in the operational regimes common in professional audio, which is why the linearity assumption (iv) can be questionable. Although significant, this aspect is out of scope for the present contribution. Another questionable postulate is that the diaphragm moves as a solid piston, assumption (i). In reality, structural modes form in the diaphragm at higher frequencies, which means that the effective moving mass will be frequency dependent, leading to an uneven frequency response. This “break-up” mechanism may lower the moving mass at higher frequencies and therefore boost the high-frequency response, which, perhaps surprisingly, sometimes is regarded as beneficial. Also, this (important) aspect will not be considered here. However, violations of assumptions (ii) and (iii) will be addressed in detail.

For real drivers, it does not hold that the acoustic pressure p is the same at each point within the chamber. In particular, the diameter of the diaphragm will typically be large enough so that acoustic modes form in the compression chamber. In fact, the positioning of the outlet, as in Figure 1, is particularly bad, mostly spoiling the effect of the compression chamber. To address this issue, Smith [16] developed an ingenious strategy that divides the outlet area S_{wg} into N circumferential slits. If these are properly placed and sized, Smith showed that the N lowest radial modes in the chamber will not be excited.

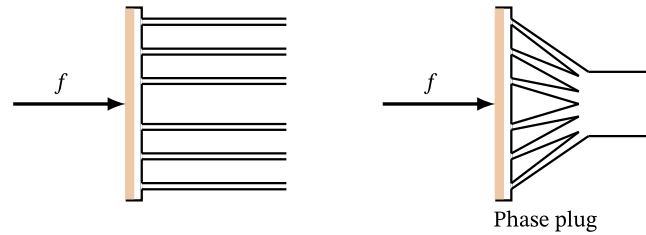


FIGURE 3 | Left: A conceptual cylindrical compression driver with annular openings, placed according to Smith’s guidelines, to suppress radial modes in the compression chamber. Right: The function of the phase plug is to guide the sound from the slits into the throat of a horn. Cross-sectional view through the axis.

An example with $N = 3$ is shown to the left in Figure 3. Such a configuration performs very closely to the ideal responses of Figure 2 in the operational range below the first $N + 1$ radial modes as long as the slits are perfectly absorbing. However, to mount the driver to the mouth of a horn, which is typically cylindrical, the slits need somehow to be connected together using a device known as a *phase plug*. Figure 3 displays, to the right, a simple design of a phase plug for $N = 3$ Smith slits attached to the compression chamber. Unfortunately, the phase plug introduces a nonideal load at the outlets from the compression chamber as well as interdependencies between the loads to each slit, which means that the radial chamber modes will not be completely suppressed. Moreover, the coupling between the slits means that internal resonances can also build up within the phase plug. In a previous contribution [21], we used gradient-based optimization to shape the phase-plug channels, which significantly improved the frequency response compared to a design as shown to the right in Figure 3, although we did not succeed in removing all resonances within the device.

As we saw in Section 2, high compression rates and narrow compression chambers are needed to obtain, for a given diaphragm movement, a high sound pressure and to avoid an excessive drop at high frequencies. The device will thus contain very narrow regions. As a consequence, the viscothermal losses generated in the boundary layers cannot be ignored, violating the isentropic assumption. This effect was noted already in the previous contribution [21], where viscothermal losses were taken into account a posteriori by solving the linearized, compressible Navier–Stokes equations. That is, the optimization was carried out using the isentropic Helmholtz equation for the acoustic pressure, but the performance of the optimized device was assessed taking viscothermal losses into account. Even though the final design outperformed the original design, this approach is conceptually unsatisfactory; it would be preferable to account for the losses also in the optimization step.

As discussed in the introduction, although the linearized, compressible Navier–Stokes equations accurately compute the lossy sound transmission, they are impractical to use for shape optimization, due to extensive computational times and the need to manage the required extreme mesh refinements in the boundary-layer region. Here, we will instead rely on the boundary-condition model discussed in the introduction. Berggren et al. [1] demonstrated the accuracy and extreme efficiency of this model on a compression driver with the same type of radial outlets as considered here. The output sound pressure when employing the new model agreed closely with the one obtained from a more complete model, in which the linearized, compressible Navier–Stokes equations were used in the compression driver and phase plug. However, the new model required about two orders of magnitude less memory and computational time compared to the more complete model. Thus, the access to the boundary-layer model makes it now possible to apply numerical shape optimization to design the phase plug of a compression driver while taking viscothermal losses into account during the optimization.

4 | The Compression Driver With Radial Slits

An alternative to the Smith slits is to orient the outlets from the compression chamber in the *radial* direction, as in Figure 4. Note that the wave propagation then is intrinsically three-dimensional, whereas 2D axial symmetry modeling is possible for circumferential slits.

The device we will consider contains N_s radial slits, placed symmetrically in the circumferential direction, and the computational domain, depicted in Figure 5, contains one of these in half symmetry, with symmetry planes Γ_{sym} placed in the radial direction. The wall Γ_p of the phase plug, shown in Figure 5 in its initial shape, is the part of the device subject to shape optimization. The phase plug connects the compression chamber, whose back side is the diaphragm Γ_d , to

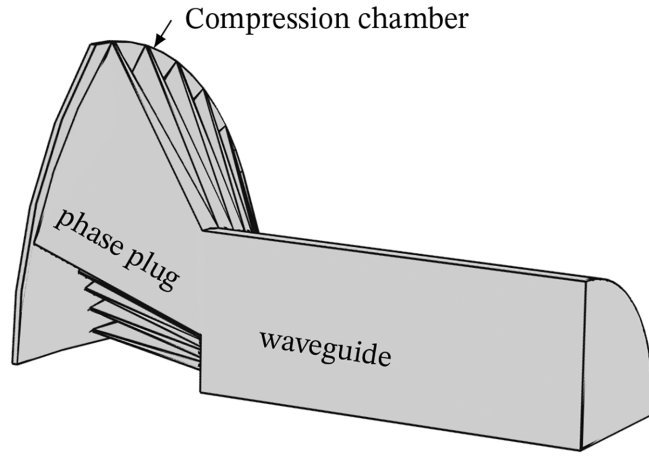


FIGURE 4 | Cutaway drawing of a compression driver with radial slits, attached to a cylindrical waveguide.

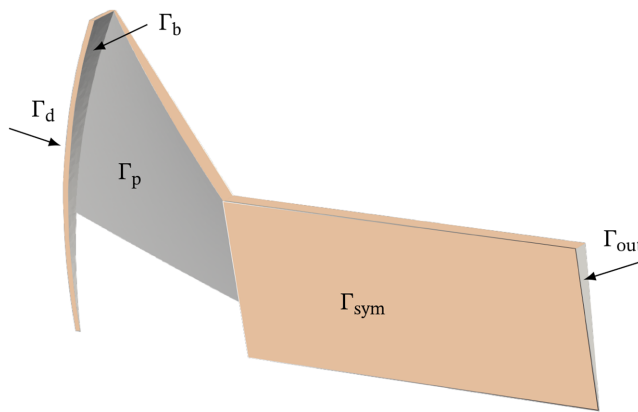


FIGURE 5 | The computational domain with the initial shape of the phase-plug wall Γ_p . A vanishing Neumann boundary condition is imposed on Γ_{sym} , consisting of the full back side together with the surfaces indicated with tinted color in the figure.

the waveguide. On the spherically-shaped diaphragm Γ_d , we impose a uniform oscillatory movement in the axial direction with angular frequency ω . This movement generates an acoustic pressure $P(\mathbf{x}, t) = \text{Re}e^{i\omega t} p(\mathbf{x})$ in the computational domain, and we require the complex pressure amplitude p function to satisfy the following boundary-value problem for the Helmholtz equation,

$$-\Delta p - k^2 p = 0 \quad \text{in } \Omega, \quad (5a)$$

$$ikp + \frac{\partial p}{\partial n} = 0 \quad \text{on } \Gamma_{out}, \quad (5b)$$

$$\frac{\partial p}{\partial n} = 0 \quad \text{on } \Gamma_{sym}, \quad (5c)$$

$$-\delta_V \frac{i-1}{2} \Delta_T p + \delta_T k^2 \frac{(i-1)(\gamma-1)}{2} p + \frac{\partial p}{\partial n} = \begin{cases} \rho_0 a_m \mathbf{n} \cdot \mathbf{e}_a & \text{on } \Gamma_d, \\ 0 & \text{on } \Gamma_w \setminus \Gamma_d, \end{cases} \quad (5d)$$

$$\mathbf{n}_T \cdot \nabla_T p = 0 \quad \text{on } \partial\Gamma_w. \quad (5e)$$

The boundary condition on the outlet Γ_{out} of the waveguide is a simple radiation condition that perfectly absorbs planar modes. In all numerical experiments, the frequency will be chosen so that all higher waveguide modes in the radial direction will be evanescent. Following Oclew-Brown's recommendations ([18], Ch. 7), we choose N_s fairly large to suppress circumferential modes in the compression chamber. To impose symmetry or, equivalently, a lossless hard-wall condition, the vanishing Neumann boundary condition (5c) is imposed on the whole back side of the domain in Figure 5 as well as on the tinted surfaces in the figure. The purpose of the waveguide with the given boundary conditions is to impose

a perfectly matched condition at the outlet of the phase plug; in reality, the outlet of the compression driver is typically directly mounted to the throat of a horn.

The viscothermal condition (5d) is imposed on Γ_w , which is the union of all remaining large solid wall surfaces: The oscillating diaphragm Γ_d , the phase plug wall Γ_p , whose shape will be subject to optimization, and the front side of the compression chamber Γ_b , which will be fixed throughout the optimization. Note, from Figure 5, that lossless homogeneous Neumann boundary conditions are imposed on the top part of the compression chamber as well as the top and bottom parts of the phase plug, although viscothermal losses would be more appropriate. This simplification streamlines the implementation and will only have a marginal acoustic effect. In particular, the top and bottom parts of the phase plug are modeled without viscothermal losses to avoid cumbersome modifications to the shape gradient in the cases where the size of these parts changes.

The coefficients in condition (5d) contain the viscous and thermal boundary-layer thicknesses

$$\delta_V = \sqrt{\frac{2\nu}{\omega}}, \quad \delta_T = \sqrt{\frac{2\lambda}{\omega\rho_0 c_p}}, \quad (6)$$

where ν and λ are the kinematic viscosity and thermal conductivity coefficient of air, respectively, and c_p is the specific heat capacity of air at constant pressure. This type of boundary condition, involving the *tangential Laplacian operator* Δ_T , can be viewed as a generalized impedance boundary condition, and is sometimes referred to as a *Wentzell* boundary condition. The tangential Laplacian operator in boundary condition (5d) generates diffusion in the tangential plane Γ_w and can be defined as

$$\Delta_T p = \nabla_T \cdot (\nabla_T p) \quad (7)$$

using the tangential gradient and tangential divergence operators

$$\nabla_T p = \nabla p - \mathbf{n} \frac{\partial p}{\partial n}, \quad \nabla_T \cdot \mathbf{q} = \nabla \cdot \mathbf{q} - \mathbf{n} \cdot \frac{\partial \mathbf{q}}{\partial n}, \quad (8)$$

defined for scalar and \mathbb{R}^3 -valued functions p and \mathbf{q} , respectively.

Indeed, condition (5d) constitutes in itself a diffusion–reaction problem on the boundary surface, coupled to the bulk Helmholtz problem (5a) through the normal flux. The presence of the tangential Laplacian requires a “boundary condition to the boundary condition”, that is, a condition on the interfaces of codimension 2 towards neighboring boundary surfaces. We impose here condition (5e), similarly as in the publication where the viscothermal model was devised [1]. Vector \mathbf{n}_T is the *conormal* field at the interfaces $\partial\Gamma_d$, $\partial\Gamma_b$, and $\partial\Gamma_p$ to the boundary surfaces involved in boundary condition (5d). (At each interface, the conormal field is outward-directed and in the tangent plane of the associated surface Γ_d , Γ_b , and Γ_p .) The forcing given on Γ_d in boundary condition (5d), in which \mathbf{e}_a is a unit vector in the axial direction, stems from the diaphragm’s oscillation with the acceleration amplitude a_d .

The variational formulation of the boundary-value problem (5), on which the finite-element discretization is based, is as follows.

$$\begin{aligned} &\text{Find } p \in W \text{ such that} \\ &a(q, p) = l(q) \quad \forall q \in W, \end{aligned} \quad (9)$$

where

$$a(q, p) = \int_{\Omega} \nabla q \cdot \nabla p - k^2 \int_{\Omega} qp + ik \int_{\Gamma_{\text{out}}} qp + \delta_T k^2 \frac{(i-1)(\gamma-1)}{2} \int_{\Gamma_w} qp + \delta_V \frac{i-1}{2} \int_{\Gamma_w} \nabla_T q \cdot \nabla_T p, \quad (10a)$$

$$l(q) = \int_{\Gamma_d} \rho_0 q a_d \mathbf{n} \cdot \mathbf{e}_a, \quad (10b)$$

where W , a strict subspace of $H^1(\Omega)$, is the closure of functions in $\mathcal{C}^1(\overline{\Omega})$ with respect to the norm devised by

$$\|p\|_W^2 = k^2 \int_{\Omega} |p|^2 + \int_{\Omega} |\nabla p|^2 + \delta_T (\gamma-1) k^2 \int_{\Gamma_w} |p|^2 + \delta_V \int_{\Gamma_w} |\nabla_T p|^2. \quad (11)$$

Note that condition (5e) is a “natural condition” for the tangential Laplacian, meaning that these interfaces will not enter into the variational formulation, analogously to the vanishing of the symmetry condition (5c). Thus, this interface will be neither a source nor a sink of acoustic power. The well-posedness proof in our previous article ([1], Appendix B) also applies to problem (9).

Remark 4.1. To save space, we will generally leave out the measure symbols in the integrals in this article, like in expressions (10) and (11). The choice of integration measure will be clear from the domain of integration.

5 | Optimization Problem

The maximal domain D of all feasible computational domains, the *hold all*, is depicted to the left in Figure 6. To describe the shape of the phase-plug boundary Γ_p , we employ a level-set function $\phi : \Omega_{p, \max} \rightarrow \mathbb{R}$, whose domain $\Omega_{p, \max} \subset D$ is the tinted part to the left in Figure 6. The complement $\Omega_0 = D \setminus \Omega_{p, \max}$, illustrated to the right in Figure 6, consists of the compression chamber, the waveguide, and a thin region on the back side of the phase plug; Ω_0 is fixed throughout the computations.

The phase-plug boundary and interior are defined through a level-set function on $\Omega_{p, \max}$ as

$$\begin{aligned} \Gamma_p &= \{ \mathbf{x} \in \Omega_{p, \max} \mid \phi(\mathbf{x}) = 0 \}, \\ \Omega_p &= \{ \mathbf{x} \in \Omega_{p, \max} \mid \phi(\mathbf{x}) < 0 \}. \end{aligned} \tag{12}$$

The level-set function will, in turn, implicitly be defined using a 3D generalization of the approach used in previous studies [21, 22]. That is, ϕ is the solution to the boundary-value problem

$$-\Delta \phi = \hat{\phi} \quad \text{in } \Omega_{p, \max}, \tag{13a}$$

$$\phi = \phi_D \quad \text{on } \partial\Omega_{p, \max}^D, \tag{13b}$$

$$\frac{\partial \phi}{\partial n} = 0 \quad \text{on } \partial\Omega_{p, \max} \setminus \partial\Omega_{p, \max}^D. \tag{13c}$$

On the part of the boundary to $\Omega_{p, \max}$ facing the compression chamber, we assign the Dirichlet boundary condition (13b); the values of ϕ_D are given by the design illustrated in Figure 5, which also serves as the initial design for the optimization. In this way, $\partial\Omega_{p, \max}^D$ will always be closed to the compression chamber, and the outlet from the compression chamber, shown as a tinted surface in the close up of the right picture in Figure 6, will be a part of Ω_0 and thus fixed throughout the computations. We made this choice to fix a priori the compression ratio to be determined by requirements not assessed with the current model. (For instance, too high compression ratios together with too narrow chambers may introduce

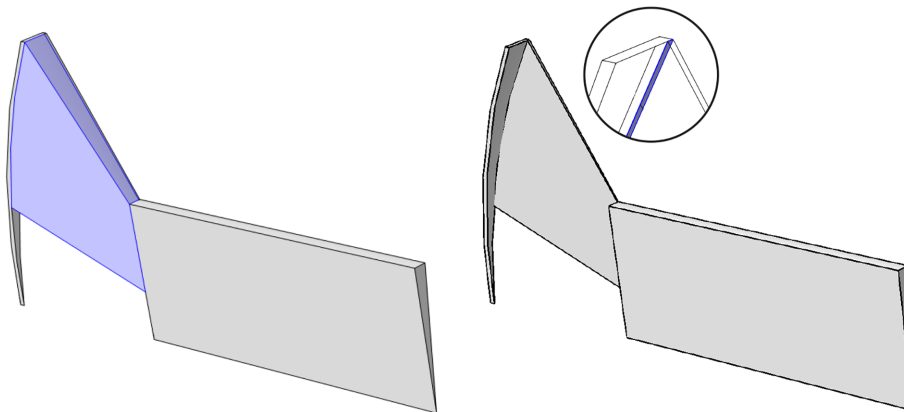


FIGURE 6 | The hold-all D is the union of the gray and tinted parts in the left picture. The domain for the level set function ϕ is the tinted (blue) part $\Omega_{p, \max}$. The part of the computational domain that is fixed is the gray part, $\Omega_0 = D \setminus \Omega_{p, \max}$, shown to the right. The tinted surface in the close-up indicates the very narrow exit from the compression chamber. The computational domain is $\Omega = \Omega_0 \cup \Omega_p$, where $\Omega_p \subset \Omega_{p, \max}$ such that $\phi < 0$.

excessive sound pressures and high distortion.) The homogeneous Neumann condition (13c) on the rest of the boundary yields freedom for the phase-plug boundary and interior to intersect the boundary of $\Omega_{p, \max}$, a property that indeed will be observed in the optimized devices. The level-set function will depend on the right-hand-side function $\hat{\phi}$, whose nodal values in $\Omega_{p, \max}$, after finite-element discretization, will be the actual design variables updated by the optimization algorithm.

The quantity of interest for the optimization is the mean sound pressure at the exit of the waveguide, that is,

$$p_{\text{out},k} = \frac{1}{|\Gamma_{\text{out}}|} \int_{\Gamma_{\text{out}}} p, \quad (14)$$

where p is the solution to variational problem (9) for wave number k , and $|\Gamma_{\text{out}}|$ the area of Γ_{out} . Due to the absorbing boundary condition on Γ_{out} and the evanescence of higher waveguide modes, the transmitted acoustic power is proportional to $|p_{\text{out},k}|^2$. For a set \mathcal{K} of wave numbers, we will compare the results of optimization using the two objective functions

$$J_{\text{pow}}(\hat{\phi}) = \frac{1}{2} \sum_{k \in \mathcal{K}} \frac{1}{|p_{\text{out},k}|^2} \quad (15)$$

and

$$J_{\text{track}}(\hat{\phi}) = \frac{1}{2} \sum_{k \in \mathcal{K}} |p_{\text{out},k} - p_{\text{out},k}^{\text{ideal}}|^2, \quad (16)$$

where

$$p_{\text{out},k}^{\text{ideal}} = p_k^{\text{ideal}} e^{-ikL}, \quad (17)$$

where p_k^{ideal} is the ideal pressure response as obtained from Equation (2) and e^{-ikL} the phase factor associated with a planar wave propagating the distance L between the diaphragm and the waveguide outlet Γ_{out} .

Thus, by minimizing J_{pow} , we are maximizing the harmonic mean of the output power at the considered wave numbers, whereas by minimizing J_{track} , we are aiming to match the frequency response to the ideal one. If needed, a Tikhonov regularization term may be added,

$$J_{\epsilon}(\hat{\phi}) = \epsilon J_{\text{T}}(\hat{\phi}) + J_{\text{obj}}(\hat{\phi}), \quad (18)$$

where J_{obj} is either of the two objectives (15) or (16), and

$$J_{\text{T}}(\hat{\phi}) = \frac{1}{2} \int_{\Omega_{d,\max}} (\hat{\phi} - \hat{\phi}_0)^2, \quad (19)$$

in which $\hat{\phi}_0$ is the right-hand side function in Equation (13a) associated with the starting guess of the optimization. Such a regularization will put a bound on how much the level-set function can change from its initial shape. In a previous study [22], we found that this type of regularization was effective in limiting the curvature of the design boundary. As we will see, in practice, it turns out that the Tikhonov regularization will not be necessary to employ in this case.

6 | Discretization

The cut finite element method (CutFEM) [23] is a discretization technique that is similar to the XFEM approach [34]. These techniques are particularly suitable for problems, like here, in which the shape of the domain is unknown in the problem to be solved [24–26, 35]. We employ a 3D version of the approach used in recent 2D acoustic shape optimization studies [21, 22].

The hold all D (Figure 6) is triangulated into a mesh \mathcal{T}_h of unstructured tetrahedra with maximum diameter $h > 0$. We require the mesh surfaces to conform with the interface between the level-set domain $\Omega_{p, \max}$ and the rest of D . Let V_h^n be the space of continuous functions that are polynomials of maximal degree n on each tetrahedron $K \in \mathcal{T}_h$. From V_h^1 , we

form the discrete space used to numerically solve the level-set boundary-value problem (13). Let $U_h = V_h^1|_{\Omega_{p,\max}}$, and let $U_{h,0}$ be the subspace of functions in U_h vanishing on $\partial\Omega_{p,\max}^D$. The discrete level set function ϕ_h will then be the solution to

$$\begin{aligned} \phi_h \in U_h \text{ such that } \phi_h = \phi_D \text{ on } \partial\Omega_{p,\max}^D, \text{ and} \\ \int_{\Omega_{p,\max}} \nabla z_h \cdot \nabla \phi_h = \int_{\Omega_{p,\max}} z_h \hat{\phi}_h \quad \forall z_h \in U_{h,0}, \end{aligned} \quad (20)$$

in which $\hat{\phi}_h \in \mathcal{U}_h$, where \mathcal{U}_h is the space of design variables in the discrete case, which we choose to be equal to the space of test functions, $\mathcal{U}_h = U_{h,0}$.

Then, analogously as in definition (12), the discrete level-set function ϕ_h defines the discrete phase-plug boundary and interior as

$$\begin{aligned} \Gamma_{p,h} &= \{ \mathbf{x} \in \Omega_{p,\max} | \phi_h(\mathbf{x}) = 0 \}, \\ \Omega_{p,h} &= \{ \mathbf{x} \in \Omega_{p,\max} | \phi_h(\mathbf{x}) < 0 \}. \end{aligned} \quad (21)$$

Note that $\Gamma_{p,h}$ in general will cut through the inside of the elements of the triangulation, and that $\Omega_{p,h}$ thus will not conform to the mesh inside $\Omega_{p,\max}$. However, since ϕ_h is piecewise linear, the surface $\Gamma_{p,h}$ will be piecewise planar. This property greatly simplifies both the assembly process for the acoustic finite-element matrices and the derivation of the shape calculus formulas for optimization.

The computational domain for the acoustic problem in the discrete case is $\Omega_h = \Omega_{p,h} \cup \Omega_0$; $\Omega_{p,h}$ will be a subset of the tinted volume ($\hat{\Omega}_{p,\max}$) in Figure 6 and Ω_0 is the part shown to the right. The finite-element approximation of the variational problem (9) will be carried out in the space

$$W_h = \{ p_h | p_h = q_h|_{\Omega_h} \text{ for some } q_h \in V_h^2 \}. \quad (22)$$

Thus, we use piecewise-quadratic functions for the acoustic problem. Note that the number of degrees of freedom for functions in W_h will depend on the location of $\Gamma_{p,h}$. Also note that for elements that are intersected by $\Gamma_{p,h}$, there will be basis function nodes for W_h located outside of $\Omega_{p,h}$. This situation is illustrated in Figure 7, for simplicity of presentation in the analogous two-dimensional case.

The finite-element approximation of problem (9) will be as follows.

$$\begin{aligned} \text{Find } p_h \in W_h \text{ such that} \\ a(q_h, p_h) + \epsilon_s s_h(q_h, p_h) = l(q_h) \quad \forall q_h \in W_h, \end{aligned} \quad (23)$$

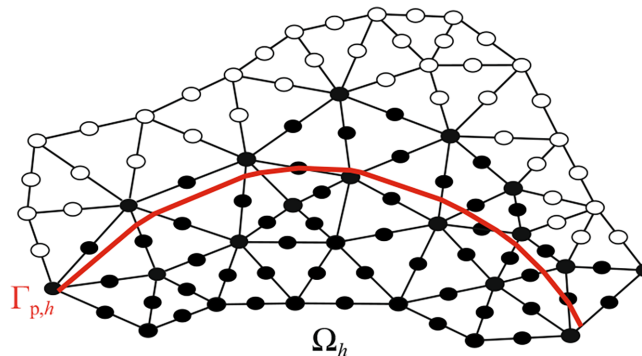


FIGURE 7 | The domain boundary $\Gamma_{p,h}$ is defined by a vanishing level set function ϕ_h . The computational domain Ω_h is here below $\Gamma_{p,h}$. The nodes marked in black will affect the solution p_h inside Ω_h , whereas the white nodes will not.

where $a(\cdot, \cdot)$ is defined as in expression (10a) but with $\Omega = \Omega_h$. The bilinear term

$$s_h(p_h, q_h) = \sum_{S \in \mathcal{S}_h^g} \int_S h^3 \llbracket \mathbf{n} \cdot \nabla p_h \rrbracket \llbracket \mathbf{n} \cdot \nabla q_h \rrbracket \quad (24)$$

is a so-called ghost penalty [23, 36], which is added to combat ill-conditioning of the system matrix in cases when only a small portion of an element intersected by $\Gamma_{p,h}$ is located inside Ω_h . Here, $\epsilon_s > 0$ is a dimensionless stabilization parameter, \mathcal{S}_h^g denotes the set of ghost penalty mesh faces, defined as the set of interior faces belonging to elements $K \in \mathcal{T}_h$ that are cut by the embedded boundary $\Gamma_{p,h}$, while $\llbracket \cdot \rrbracket$ denotes the jump of sufficiently smooth, element-wise defined functions across a face S . More precisely, let \mathbf{f} be a vector-valued function, satisfying $\mathbf{f}|_K \in C^0(\overline{K})^3$ for each $K \in \mathcal{T}_h$. Moreover, let $K_1, K_2 \in \mathcal{T}_h$ be two elements sharing the mesh face S . For any $\mathbf{x} \in S$ and for $i = 1, 2$, we define the limit functions

$$\mathbf{f}_i(\mathbf{x}) = \lim_{t \rightarrow 0^+} \mathbf{f}(\mathbf{x} - t\mathbf{n}_i), \quad (25)$$

where \mathbf{n}_i is the outward-directed normal to K_i on S . Thus, $\mathbf{f}_1(\mathbf{x}) = \mathbf{f}_2(\mathbf{x})$ only if \mathbf{f} is continuous at \mathbf{x} . Then the jump expression can be defined as

$$\llbracket \mathbf{n} \cdot \mathbf{f}(\mathbf{x}) \rrbracket = \mathbf{n}_1 \cdot \mathbf{f}_1(\mathbf{x}) + \mathbf{n}_2 \cdot \mathbf{f}_2(\mathbf{x}). \quad (26)$$

Since $\mathbf{n}_1 = -\mathbf{n}_2$ on S , definition (26) indeed indicates a jump in the normal derivative of \mathbf{f} at S .

The presence of ghost-penalty term s_h does not affect the consistency of finite-element approximation (23), since it vanishes for sufficiently smooth p , where p is the solution to variational problem (9).

Remark 6.1. Even though the number of active degrees of freedom in the problem (23) changes with the location of $\Gamma_{p,h}$, it may be practical to keep the number of degrees fixed in the implementation. A fixed number of degrees of freedom is easily accomplished by extending all functions in W_h into V_h by enlarging the system by an identity matrix and a zero right hand side for the degrees of freedom not affecting $p_h|_{\Omega_h}$; in Figure 7 the solution would then vanish at the white nodes.

Replacing $p_{\text{out},k}$ in the definitions of objective functions (15), (16), and (18) with the corresponding numerical solution obtained from Equation (23), we arrive at the following discrete optimization problem:

$$\begin{aligned} &\text{Find } \hat{\phi}_h^* \in \mathcal{U}_h \text{ such that} \\ &J_\epsilon(\hat{\phi}_h^*) \leq J_\epsilon(\hat{\phi}_h) \quad \forall \hat{\phi}_h \in \mathcal{U}_h. \end{aligned} \quad (27)$$

7 | Shape Calculus

An evaluation of the function $\hat{\phi}_h \mapsto J_{\text{obj}}$ involves a composition of several operations,

$$\hat{\phi}_h \mapsto \phi_h \mapsto \Omega_h \mapsto p_h \mapsto p_{\text{out},k} \mapsto J_{\text{obj}}. \quad (28)$$

That is, each function $\hat{\phi}_h$ gives rise to a level set function ϕ_h through the solution of problem (20), which in turn through definition (21) yields the computational domain Ω_h for problem (23). Solutions to problem (23) provide the acoustic pressures for each wavenumber, the quantities of interest $p_{\text{out},k}$ in definition (14), and finally J_{obj} , either in terms of the power (15) or the tracking (16) objective function. To compute derivatives to be used by the optimization algorithm, we thus need to apply the chain rule to the composition (28).

We have reported a shape calculus using the same kind of composition in earlier contributions [21, 22], except that the previous studies were done in 2D and without the boundary-layer model. Apart from the mapping $\Omega_h \mapsto p_h$, previous calculations apply with minor adjustments. However, the presence of the integrals over $\Gamma_{w,h}$ arising from the boundary-layer model in the discretization of bilinear form (10a) significantly alters the shape calculus for this part of the mapping. Tisot, Billard, and Garbard [10] carry out shape calculus for a conceptually similar case, that is, using a level-set geometry representation, cut elements, and the same viscothermal boundary-layer model. However, their shape calculus relies on the classic formula (B7) discussed in Appendix B, which requires a smoothness that does not hold in the current case. For instance, since the level-set function is continuous and piecewise linear, the design boundary will be continuous and

piecewise planar but not C^2 , and thus its curvature, which enters in Formula (B7), can only be defined discretely as jumps of the normal field between element surfaces. In addition, the smoothness assumption on the integrand, $f \in W^{1,1}(D)$, does not hold in our case either.

Instead, we will rely on a more general set of formulas discussed in Appendix B. Here, we summarize the steps involved in computing the derivative of the mapping from the level-set function to the average acoustic pressure at the outlet

$$j(\phi_h) = p_{\text{out},k} = \frac{1}{|\Gamma_{\text{out}}|} \int_{\Gamma_{\text{out}}} p_h, \quad (29)$$

and refer to Appendix B for the derivation of the expressions. Note that $p_{\text{out},k}$ is a complex number, and that the final objective function J_{obj} (expression (15) or (16)) is of least-squares type, involving a sum of squares over frequencies and over the real and imaginary parts.

The continuous, piecewise-linear level-set function ϕ_h can be expanded in a Lagrangian basis $\{w_i\}_{i=1}^M$. Letting w_l , for $l \in \{1, \dots, M\}$, be any of the basis functions of the expansion, we introduce the family of perturbations

$$\phi_h^t = \phi_h + tw_l, \quad (30)$$

parametrized by $t \in \mathbb{R}$. The current study only addresses *shape* changes of the phase-plug wall. In particular, we do not aim to alter the topology of the device. We may thus assume that all phase-plug boundaries are manifolds of codimension one; that is, the level-set function vanishes only on a surface, not at isolated points, nor in a region of positive measure. For parameter t small enough, the perturbation therefore generates a family of perturbed phase-plug wall boundaries and interiors

$$\begin{aligned} \Gamma_{p,h}^t &= \{ \mathbf{x} \in \Omega_{p,\max} | \phi_h^t(\mathbf{x}) = 0 \}, \\ \Omega_{p,h}^t &= \{ \mathbf{x} \in \Omega_{p,\max} | \phi_h^t(\mathbf{x}) < 0 \}, \end{aligned} \quad (31)$$

and the directional derivative of objective function (29) is defined as

$$dj(\phi_h; w_l) = \lim_{t \rightarrow 0} \frac{j(\phi_h + tw_l) - j(\phi_h)}{t}. \quad (32)$$

Remark 7.1. Even if the level-set function initially only vanishes on a surface, we have not here provided any mechanism to *guarantee* that this property is retained throughout the optimization, since there has been no need for it in this study. However, for other optimization problems, there may be a need to monitor and occasionally reinitialize the level-set function using algorithms developed for this purpose [37].

In most cases, we expect $\Gamma_{p,h}$ to cut through the interior of the mesh cells. However, if ϕ_h happens to vanish along a mesh face, then this part of $\Gamma_{p,h}$ will coincide with that mesh face. This is a rather exceptional case, unlikely to emerge during the optimization iterations, since it means that the degrees of freedom for ϕ_h restricted on that mesh face happen to be updated so that the level-set function vanishes exactly on that face. However, in that specific case, at most one-sided versions of directional derivative (32) can be expected to hold for the particular basis functions w_l associated with this mesh face. Thus, we exclude this case here as well as in the derivation in Appendix B, an exclusion further motivated by the fact that we did not experience any effects of this possible nonsmoothness in the numerical studies.

Multiple times in the following, we will need to refer to the integrand for the terms in the variational form responsible for the modeling of viscothermal losses, that is, the terms in the integral over Γ_w in definition (10a). Thus, for convenience, we will introduce the notation

$$\begin{aligned} \psi(q, p; \mathbf{n}) &= \delta_T k^2 \frac{(i-1)(\gamma-1)}{2} qp + \delta_V \frac{i-1}{2} \nabla_T q \cdot \nabla_T p \\ &= \delta_T k^2 \frac{(i-1)(\gamma-1)}{2} qp + \delta_V \frac{i-1}{2} (\nabla q \cdot \nabla p - \mathbf{n} \cdot \nabla q \mathbf{n} \cdot \nabla p). \end{aligned} \quad (33)$$

Note that the dependency of ψ on \mathbf{n} is due to the definition (8) of the tangential gradient.

As outlined in Section 6, given a particular level-set function $\phi_h \in U_h$, the discrete acoustic pressure $p_h \in W_h$ is the solution of the finite-element problem

$$a(q_h, p_h) + \epsilon_h s_h(q_h, p_h) = l(q_h) \quad \forall q_h \in W_h. \quad (34)$$

Letting $z_h \in W_h$ be the solution of the adjoint equation

$$a(w_h, z_h) + \epsilon_h s_h(w_h, z_h) = \int_{\Gamma_{\text{out}}} w_h \quad \forall w_h \in W, \quad (35)$$

the directional derivative (32) can be computed, with a notation explained below, from

$$\begin{aligned} dj(\phi_h; w_l) = & \int_{\Gamma_{p,h}} (\nabla z_h \cdot \nabla p_h - k^2 z_h p_h) \frac{w_l}{|\partial_n \phi_h|} \\ & + \delta_V \frac{i-1}{2} \int_{\Gamma_{p,h}} \left(\frac{(P_T \nabla w_l) \cdot \nabla z_h}{|\partial_n \phi_h|} \frac{\partial p_h}{\partial n} + \frac{\partial z_h}{\partial n} \frac{(P_T \nabla w_l) \cdot \nabla p_h}{|\partial_n \phi_h|} \right) \\ & + \int_{\Gamma_{p,h}} \frac{\partial}{\partial n} \psi(z_h, p_h; \mathbf{n}) \frac{w_l}{|\partial_n \phi_h|} + \sum_{S \in \mathcal{S}_h} \int_{\Gamma_{p,h} \cap S} \mathbf{n}^S \cdot \llbracket \psi(z_h, p_h; \mathbf{n}) \mathbf{m} \rrbracket \frac{w_l}{|\partial_n \phi_h|}, \end{aligned} \quad (36)$$

where $P_T = I - \mathbf{n} \otimes \mathbf{n}$ is the projector on the tangent plane of $\Gamma_{p,h}$, and where in the denominators, we use the shorthand notation ∂_n for the normal derivative. The last term in expression (36) is of a sum over the set \mathcal{S}_h of mesh faces, and the integral is evaluated over the intersection between the boundary and the mesh surfaces. Since we have assumed that no mesh surface coincides with a boundary portion, these intersections are all line segments. Figure 8 illustrates a typical case, where it is to the left and right two mesh elements $K_1, K_2 \in \mathcal{T}_h$ sharing the mesh face S , marked gray. By assumption, the phase-plug boundary $\Gamma_{p,h}$ passes through the interior of the mesh elements, and the piecewise-constant normal field \mathbf{n} restricted on $\Gamma_{p,h} \cap K_1$ and $\Gamma_{p,h} \cap K_2$ is indicated in the figure. The integration domain $\Gamma_{p,h} \cap S$ is here the red dashed line segment. The vector \mathbf{n}^S is normal to $\Gamma_{p,h} \cap S$ and in the plane S . The conormal \mathbf{m}_1 is the vector in the plane $\Gamma_{p,h} \cap K_1$ and outward-directed from K_1 and normal to $\Gamma_{p,h} \cap S$; analogous conditions hold for \mathbf{m}_2 . If $\Gamma_{p,h} \cap K_1$ and $\Gamma_{p,h} \cap K_2$ are coplanar, then $\mathbf{m}_2 = -\mathbf{m}_1$. The conormals can be used to define limits on $\Gamma_{p,h} \cap S$ of functions on $\Gamma_{p,h}$ with jump discontinuities over element boundaries. That is, for $f : \Gamma_{p,h} \rightarrow \mathbb{R}$ such that, for $i = 1, 2$, $f|_{\Gamma_{p,h} \cap K_i} \in C^0(\Gamma_{p,h} \cap \overline{K_i})$, we define, for each $\mathbf{x} \in \Gamma_{p,h} \cap S$

$$f_i(\mathbf{x}) = \lim_{t \rightarrow 0^+} f(\mathbf{x} - t \mathbf{m}_i). \quad (37)$$

Finally, the symbol $\llbracket \cdot \rrbracket$ in the last term of expression (36) denotes a jump of its argument over $\Gamma_{p,h} \cap S$, defined, analogously as in definition (26), by

$$\llbracket \psi \mathbf{m} \rrbracket = \psi_1 \mathbf{m}_1 + \psi_2 \mathbf{m}_2. \quad (38)$$

We note that the first term of ψ in definition (33) will be continuous over $\Gamma_{p,h} \cap S$ but not, in general, the second.

Remark 7.2. Note that we use, with a slight abuse of notation, the same symbol $\llbracket \cdot \rrbracket$ for different kinds of jumps over a face S shared by two neighboring elements. In definition (26), the jump is with respect to limits associated with the normal to S , whereas in definition (38), the limits are associated with the conormals, at S , of the surface $\Gamma_{p,h}$ intersecting S .

Remark 7.3. The directional derivative expression (36) is rather long and involved, so it is reasonable to ask whether automatic (also called *algorithmic*) differentiation (AD) [38] could be used to bypass the complications. A *naive* use of AD on the computer program evaluating the mapping (28), or parts of it, is ill-advised. A straightforward use of forward-mode AD will be extremely computationally expensive due to the large number of design variables. Likewise, the backward mode may suffer from excessive memory requirements. A computationally efficient way would be to selectively use AD only for the really complicated parts, that is, those that require differentiation of the level-set function and the use of Theorems B.1 and B.3. Such a strategy is discussed by Wegert et al. [33] in an article that appeared after submission of the present manuscript. In our case, to carry out differentiation of the crucial mapping $\phi_h \mapsto p_{\text{out},k}$, the following approach could be used. Introduce first a Lagrangian consisting of the objective function minus the real part of the variational form of the state equation. Then substitute the test function in the state equation with the solution of the adjoint equation (35),

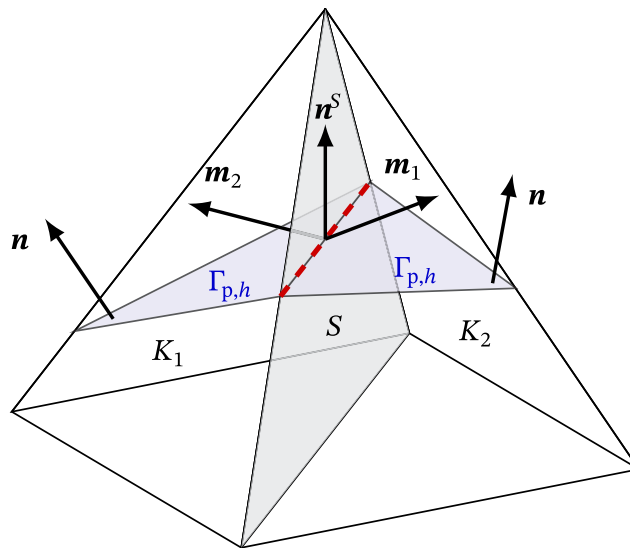


FIGURE 8 | Illustration of the geometrical objects involved in the evaluation of the last term in the directional-derivative expression (36).

whose formulation is straightforward to infer a priori. Finally, apply forward AD with respect to perturbations to the resulting Lagrangian of the nodal values of the level set function ϕ_h . Such an AD will in one sweep produce numerical values, exact up to roundoff, of the directional derivative (36) for each basis function w_j . The computational cost for this use of AD would roughly correspond to one global finite-element assembly. It would be very interesting to evaluate such an approach in a suitable computational framework to assess the possible overhead of such an automation compared to the present approach.

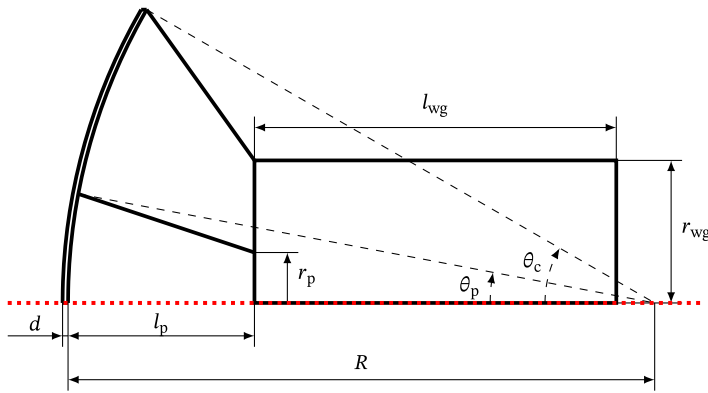
8 | Test Case Specification and Numerical Results

The compression driver we consider, illustrated in Figure 4, is equipped with $N_s = 32$ identical radial channels, and the computational domain is shown in Figure 5. The hold-all D , depicted in Figure 6, is constructed by rotating the planar domain in Figure 9 the angle $\theta_D = \pi/32$ around the dotted axial line. The thin gray backside of the phase plug visible to the right in Figure 4 is obtained by rotating the corresponding planar part in Figure 9 the angle $\theta_0 = 9.3773 \cdot 10^{-3}$ to fix the compression ratio to $\kappa = 12$. The depth of the compression chamber is $d = 0.5$ mm. The dimensions are chosen to be suitable as a driver for a horn operating in the upper midrange, 3.75–15 kHz, in the audio spectrum. Table 1 lists the air properties that are used in all computations to define the boundary-layer thicknesses (6). As mentioned in Section 1.1, our viscothermal model relies on boundary-layer theory and thus requires that the boundary layers from opposing walls do not overlap. The right picture in Figure 6 illustrates, in half symmetry, the thinnest possible achievable structure. The minimum wall distances are therefore 0.5 mm in the compression chamber and, as can be computed from the data in Figure 9, 0.2–0.5 mm (low to high position) in the phase plug. However, in the frequency range we consider, the maximum boundary layer thickness is 0.04 mm, about one order of magnitude lower than the minimum wall distance. Therefore, we consider the assumption of nonintersecting boundary layers to be sufficiently satisfied.

The computations are carried out using the FEniCS computing platform [39] in combination with our in-house library extension `libCutFEM`, which implements the CutFEM-related algorithms described by Burman et al. [25].

8.1 | Baseline

For the baseline case, we fix a level set function ϕ_h that yields the phase plug design of Figure 5. Here, the phase-plug wall $\Gamma_{p,h}$ is a surface that attaches to the edge between the compression chamber and the thin phase plug back wall and, on the other side, to the front edge of the waveguide in Figure 6. Using the air properties of Table 1 and holding the diaphragm oscillation amplitude a_d constant, we solve problem (23) in the frequency range 3.75–15 kHz with as well as without the boundary loss model, the latter achieved simply by setting $\delta_T = \delta_V = 0$, in which case the model yields the standard hard-wall vanishing Neumann boundary condition, as is clear from expression (5d). For a given, fixed value of the



θ_c	$\pi/6$	d	0.5 mm
r_{wg}	13 mm	l_{wg}	33 mm
l_c	28 mm	l_{cp}	10 mm
r_p	4.6 mm	l_p	17 mm
R	l_c/θ_c	θ_p	l_{cp}/R

FIGURE 9 | Cross section of the maximal domain.

TABLE 1 | The air properties used in all computations.

Speed of sound	c_0	343.20 m s ⁻¹
Air density	ρ_0	1.2044 kg m ⁻³
Kinematic viscosity	ν	1.5061×10^{-5} m ² s ⁻¹
Prantdl number	N_{Pr}	0.7078
Specific heat, constant pressure	c_p	1.0049 kJ kg ⁻¹ K ⁻¹
Heat capacity ratio	γ	1.4
Thermal conductivity	λ	$c_p \mu / N_{Pr}$

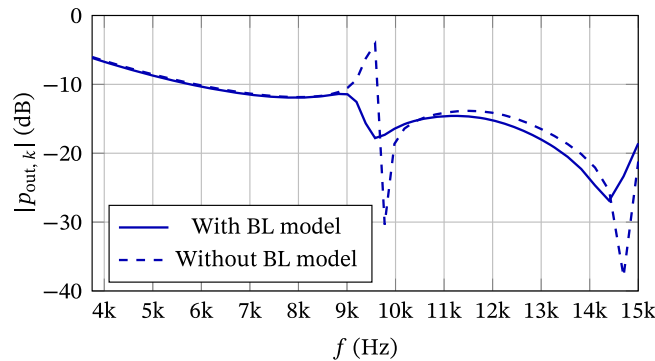


FIGURE 10 | Frequency response for the baseline design of Figure 5, with and without the boundary loss model.

diaphragm acceleration a_d , Figure 10 shows the frequency response in terms of the absolute value of the acoustic pressure at the outlet of the waveguide, $|p_{out,k}|$. Two major resonances occur at 9–10 kHz and 14–15 kHz, respectively, both of which are significantly damped by viscothermal losses. Thus, viscothermal effects cannot be neglected for frequencies higher than about 9 kHz in this case.

Remark 8.1. Similarly, as already pointed out in Remark 2.2, Figure 10 does not show a realistic frequency response of a full compression driver system, and neither will the response curves computed below for the optimized designs. The calculation of realistic system frequency responses would require a coupled model, including also the electromechanics of the transducer and a more realistic load at the waveguide. However, the purpose of the present study is to isolate the effects of the phase plug, not to simulate realistic frequency responses.

8.2 | Optimization

The optimization is carried out using the BFGS quasi-Newton algorithm as implemented in the SciPy Python library. The number of design variables, that is, the number of nodal values of the right-hand functions $\hat{\phi}_h$ in Equation (20), is 4701.

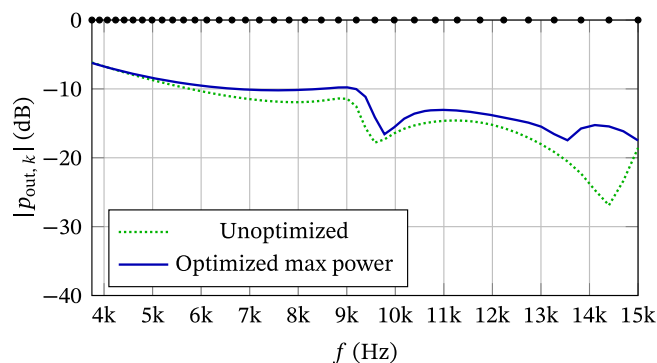


FIGURE 11 | Using objective function (15): Maximizing the harmonic mean of the output power at the 35 frequencies marked with black dots.

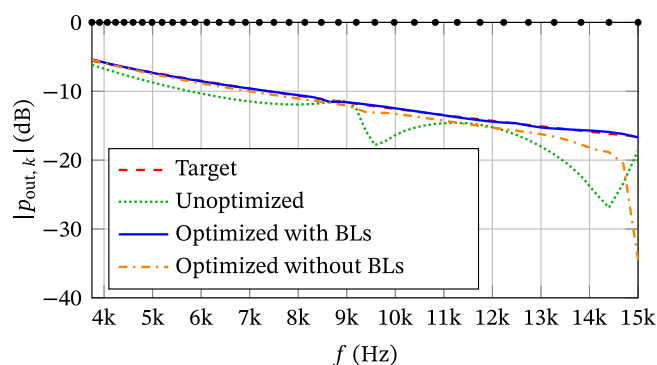


FIGURE 12 | Using objective function (16): Tracking the ideal frequency response at the 35 frequencies marked with black dots.

The stopping criterion used is when the infinity norm of the gradient of the objective function is less than 10^{-3} times its initial value. The number of iterations of the optimization algorithms was in the range 80–150.

Figure 11 shows the frequency response of the optimized device when using the objective function (15), that is, when maximizing the harmonic mean of the sound pressure $|p_{\text{out},k}|$ at the waveguide outlet. The mean is calculated over the 35 frequencies indicated with black dots in Figure 11 in the frequency range [3.75, 15] kHz; each frequency is $2^{1/17}$ times the previous frequency. The evaluation of the performance was done with the tighter frequency span of 69 frequencies, each pair spaced by the factor $2^{1/34}$. The same frequency values for optimization and evaluation are used in all the subsequent cases below. We note that the sound-pressure level is generally improved in the optimized device compared to the baseline. However, the two resonances of the baseline are still clearly noticeable, also in the optimized device.

This result indicates that a pure maximization of the sound pressure level may not be entirely satisfactory. A better strategy could be to somehow give the optimization algorithm an incentive to reduce resonance and interference effects. Therefore, it makes sense to consider the tracking approach to minimize the objective function (16). Since the frequency response based on formula (2) is the best that can be achieved under the idealized condition of ignoring wave interference effects, we expect the optimization to counteract the interference effects to be able to track the idealized response. Figure 12 shows the response of the baseline design in dotted green, the target frequency response p_k^{ideal} from expression (17) in dashed red, and the response of the optimized device in solid blue using the tracking objective function (16). The result is rather remarkable; the frequency response follows the ideal one very closely, without any noticeable resonance effects.

In the previous 2D study using radial phase plug slits [21], the optimization was performed neglecting the viscothermal losses; these losses were accounted for only afterwards when evaluating the performance of the optimized device. To evaluate the necessity of the viscothermal model during optimization, we carried out the analogous strategy here. We consider the more successful tracking approach again, optimizing using the objective function (16). The dash-dotted orange curve in Figure 12 shows the frequency response, evaluated using the viscothermal model but optimized without it. The frequency response corresponds well with the ideal response at the lower end of the spectrum, but deviates significantly at the high end. In a practical device, such a drop off at the high end would be a significant drawback. The poor

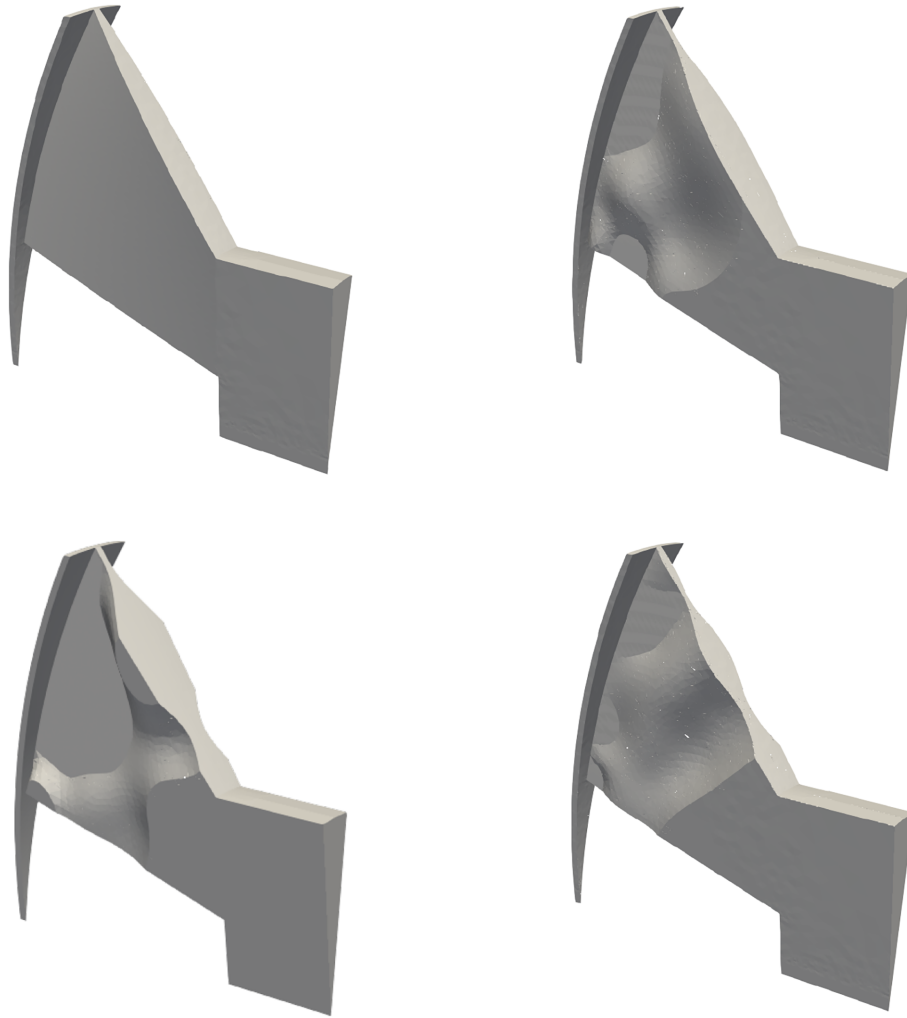


FIGURE 13 | Phase plug shapes. Baseline (top left), optimized for maximum acoustic pressure at the waveguide outlet (top right), optimized by tracking the ideal response (bottom left), optimized by tracking the ideal response while ignoring the viscothermal losses during the optimization phase.

high-frequency sensitivity would necessitate either extreme equalization, with the risk of added distortion, or the costly inclusion of an additional loudspeaker covering the highest frequencies.

The shapes of all the considered phase plugs are visualized in Figure 13, where the design is mirrored along the symmetry plane. The use of the homogeneous Neumann condition (13c) in the boundary-value problem for the level-set function implies that the level-set function may intersect the boundary of $\Omega_{p, \max}$. From Figure 13, we see that this freedom is indeed utilized in all of the optimized designs. In all of the optimized designs, note that neighboring phase plugs will be acoustically connected at the planar sections of the phase plug walls shown in Figure 13.

8.3 | Mesh Studies

The computational mesh used to carry out the computations reported above was created in Comsol Multiphysics, exported, and then imported into FEniCS. The mesh was created fine enough for the wave propagation to be well resolved. In the waveguide, the maximum edge length (h_{\max}) is 3.5 mm, which can be compared with the smallest wavelength that we considered, 22.9 mm, at 15 kHz. (Recall also that we use a second-order element for the acoustic pressure.) In the other parts of the device, the mesh is finer; the compression chamber contains at least two layers of elements with a maximal edge length of about 0.4 mm, and the maximum edge length in $\Omega_{p, \max}$, the domain of definition for the level set function, is 0.64 mm for the results presented above.

However, in addition to the issue of resolving the wave propagation, the mesh resolution in $\Omega_{p, \max}$ will also limit the achievable geometric complexity of the phase plug wall. To check the sensitivity of the computational results to the mesh resolution in the phase plug, we carried out the optimization using the tracking objective function (16) for three different meshes: The *regular* one used above, a *coarsened*, and a *refined* mesh. Viscothermal losses were taken into account in the optimization. Thus, this study corresponds to the results reported in Figure 12 and visualized in the lower left picture of Figure 13.

These meshes were created in a multiple-step procedure. First, the back side surface of the phase plug was divided into 25×32 , 36×45 , and 50×64 quadrilateral elements for the coarsened, regular, and refined meshes, respectively. (The numbers refer to the axial \times radial directions.) Between each mesh, there is about a factor of $\sqrt{2}$ in the number of elements along each side. In a second step, these surface meshes were extruded into a two-layer volume hexahedral mesh forming the fixed back plate of the phase plug, visible to the right in Figure 6. Then these hexahedra were split to form tetrahedral meshes in the back plate phase plug. In a third step, the unstructured meshes covering the rest of the computational domain were created. The meshes in $\Omega_{p, \max}$, the tinted region illustrated to the left in Figure 6, again differed by about a factor of $\sqrt{2}$ in maximal edge length. Data for the different meshes are given in Table 2. The meshes in the compression chamber and waveguide were not subject to mesh resolution studies. Figure 14 shows the results of the mesh study.

The performances are very similar between the meshes, and the designs exhibit a comparable overall structure. Thus, we conclude that the mesh used in Section 8.2 seems sufficiently fine.

TABLE 2 | Mesh data for domain $\Omega_{p, \max}$.

	Coarsened	Regular	Refined
h_{\max} (mm)	0.90	0.64	0.45
# of mesh vertices	2351	4991	11,497
# of tetrahedrons	8667	20,587	52,527
# of design variables	2054	4701	11,121

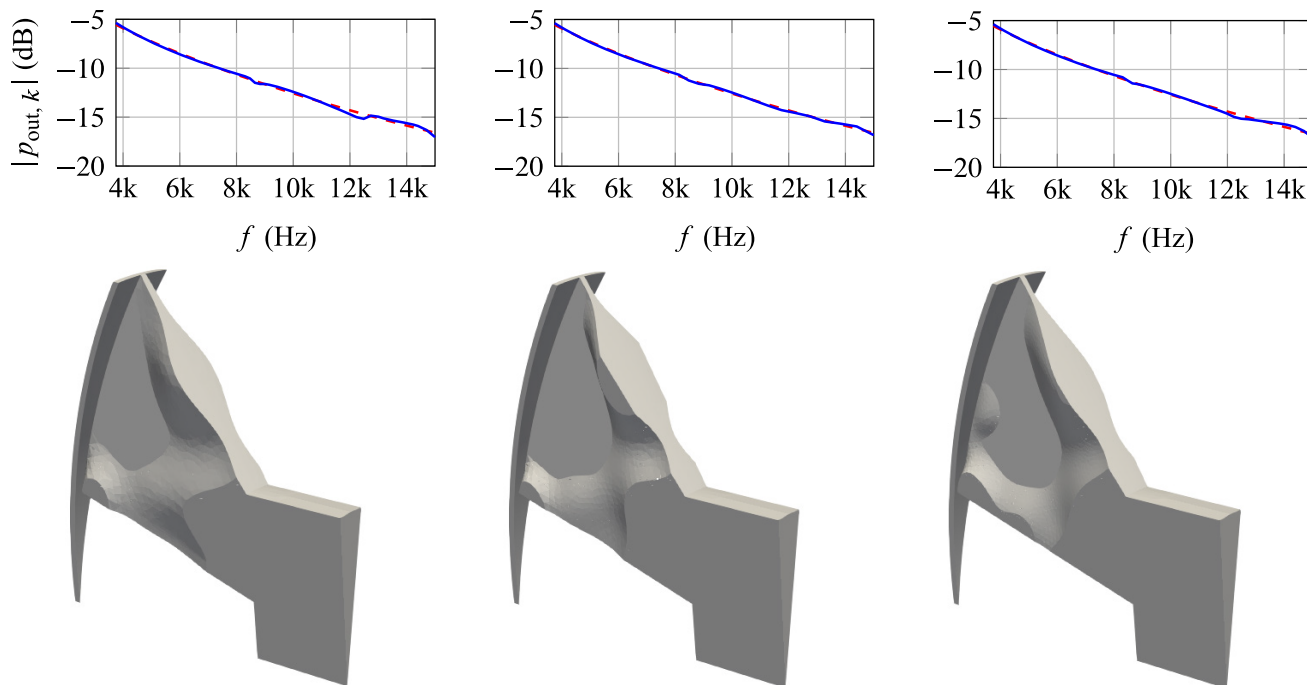


FIGURE 14 | Optimized shapes and corresponding performance for coarsened, regular, and refined meshes (left to right). Objective function (16) with dashed curve indicating target ideal response.

9 | Discussion and Conclusions

Informal discussions with experts in the design and manufacturing of compression drivers have made it clear that the radial phase plug concept is rarely used in today's commercially available compression drivers, likely due to a lack of design guidelines as straightforward as those for annular channels. Therefore, the use of numerical optimization techniques for shaping phase plugs is particularly interesting for this case. Perhaps surprisingly, when comparing with the results of shape optimization of annular channels [21], it seems like it may be easier for the optimization to find an essentially resonance-free design for radial channels, which may serve as an incentive for the industry to take a new interest in this arrangement.

Crucially important in obtaining the current results are two rather recent advances in basic modeling and optimization techniques: First, for acoustic wave propagation in the narrow geometries inside a compression driver, it is necessary to account for viscothermal losses, also during the optimization, as shown by our reported results. The recent popularization of the use of the Wentzell, or generalized impedance, condition to model viscothermal losses [1], is therefore a crucial component to be able to carry out the current study with a reasonable computational effort. A second advance utilized in this study is the combination of CutFEM methods with level-set geometry descriptions. In an earlier publication addressing the design of acoustic horns, we have shown that this approach gives exceptional design flexibility and may therefore find better designs than competing approaches [22]. To obtain accurate gradient directions for rapid convergence of the optimization algorithm, we aim for an exact shape calculus for the discrete objective function, taking into account the lack of full regularity in the phase-plug wall geometry as well as the computed acoustic pressures. However, the fact that the viscothermal losses need to be modeled on the surfaces subject to design leads to complications in the shape calculus. As far as we are aware, a fully discrete shape calculus involving the viscothermal boundary integral terms has not previously been carried out. The analysis reported in Appendix B uses a recent publication proving the relevant basic differentiation formulas [32].

Acknowledgments

Partial support for this work was provided by the Swedish Research Council, grant 2018-03546, and by eSENCE, a strategic collaborative eScience program funded by the Swedish Research Council. The computations were performed on resources provided by the Swedish National Infrastructure for Computing (SNIC) at the High Performance Computing Center North (HPC2N).

Funding

This work was supported by Vetenskapsrådet (Grant No. 2018-03546) and eSENCE, the Swedish e-Science strategic collaborative research programme.

Data Availability Statement

The data that support the findings of this study are available from the corresponding author upon reasonable request.

References

1. M. Berggren, A. Bernland, and D. Noreland, "Acoustic Boundary Layers as Boundary Conditions," *Journal of Computational Physics* 371 (2018): 633–650.
2. R. Kampinga, "Viscothermal Acoustics Using Finite Elements. Analysis Tools for Engineers," PhD Thesis, University of Twente, Enschede, The Netherlands (2010).
3. Y. Noguchi and T. Yamada, "Topology Optimization for Acoustic Structures Considering Viscous and Thermal Boundary Layers Using a Sequential Linearized Navier–Stokes Model," *Computer Methods in Applied Mechanics and Engineering* 394 (2022): 114863.
4. P. R. Andersen, V. C. Henriquez, and N. Aage, "Shape Optimization of Micro-Acoustic Devices Including Viscous and Thermal Losses," *Journal of Sound and Vibration* 447 (2019): 120–136.
5. P. R. Andersen, V. C. Henriquez, and N. Aage, "On the Validity of Numerical Models for Viscothermal Losses in Structural Optimization for Micro-Acoustics," *Journal of Sound and Vibration* 547 (2023): 117455.
6. S. Preuss, M. Paltorp, A. Blanc, V. Cutanda Henriquez, and S. Marburg, "Revising the Boundary Element Method for Thermoviscous Acoustics: An Iterative Approach via Schur Complement," *Journal of Theoretical and Computational Acoustics* 31, no. 4 (2023): 2350015.
7. H. Tijdeman, "On the Propagation of Sound Waves in Cylindrical Tubes," *Journal of Sound and Vibration* 39, no. 1 (1975): 1–33.

8. R. Christensen, "Topology Optimization of Thermoviscous Acoustics in Tubes and Slits With Hearing Aid Applications," in *Comsol Conference 2017* (Comsol, 2017), <https://www.comsol.com/paper/topology-optimization-of-thermoviscous-acoustics-in-tubes-and-slits-with-hearing-aid-applications-48751>.
9. M. J. Cops, J. G. McDaniel, E. A. Magliula, D. J. Bamford, and M. Berggren, "Estimation of Acoustic Absorption in Porous Materials Based on Viscous and Thermal Boundary Layers as Acoustic Boundary Conditions," *Journal of the Acoustical Society of America* 148, no. 3 (2020): 1624–1635.
10. G. Tissot, R. Billard, and G. Gabard, "Optimal Cavity Shape Design for Acoustic Liners Using Helmholtz Equation With Visco-Thermal Losses," *Journal of Computational Physics* 402 (2020): 109048.
11. S. B. Dilgen, N. Aage, and J. S. Jensen, "Three Dimensional Vibroacoustic Topology Optimization of Hearing Instruments Using Cut Elements," *Journal of Sound and Vibration* 532 (2022): 116984.
12. A. Mousavi, M. Berggren, and E. Wadbro, "Extending Material Distribution Topology Optimization to Boundary-Effect-Dominated Problems With Applications in Viscothermal Acoustics," *Materials & Design* 234 (2023): 112302.
13. A. Mousavi, M. Berggren, L. Hägg, and E. Wadbro, "Topology Optimization of a Waveguide Acoustic Black Hole for Enhanced Wave Focusing," *Journal of the Acoustical Society of America* 155 (2024): 742–756.
14. C. R. Hanna and J. Slepian, "The Function and Design of Horns for Loudspeakers," *Journal of the Audio Engineering Society* 25, no. 6 (1977): 573–585.
15. B. Kolbrek and T. Dunker, *High Quality Horn Loudspeaker Systems. History, Theory and Design* (Kolbrek elektroakustikk, 2019).
16. B. H. Smith, "An Investigation of the Air Chamber of Horn Type Loudspeakers," *Journal of the Acoustical Society of America* 25, no. 2 (1953): 305–312, <https://doi.org/10.1121/1.1917553>.
17. M. Dodd, "The Development of a Forward Radiating Compression Driver by the Application of Acoustic, Magnetic and Thermal Finite Element Methods," in *Audio Engineering Society Convention*, vol. 115 (Audio Engineering Society, 2003), 5886, <http://www.aes.org/e-lib/browse.cfm?elib=12445>.
18. J. Oclew-Brown, "Loudspeaker Compression-Driver Phase-Plug Design," PhD Thesis, University of Southampton, Institute of Sound and Vibration Research (2012), <https://eprints.soton.ac.uk/348798/>.
19. A. Voishvillo, *Audio Engineering Society Convention. Convention Paper 9618*, vol. 141 (Audio Engineering Society, 2016), <https://www.aes.org/e-lib/browse.cfm?elib=20375>.
20. A. Bezzola, "Numerical Optimization Strategies for Acoustic Elements in Loudspeaker Design," in *Audio Engineering Society Convention. Convention Paper 10046*, vol. 145 (Audio Engineering Society, 2018), <https://www.aes.org/e-lib/browse.cfm?elib=19772>.
21. A. Bernland, E. Wadbro, and M. Berggren, "Shape Optimization of a Compression Driver Phase Plug," *SIAM Journal on Scientific Computing* 41, no. 1 (2019): B181–B204, <https://doi.org/10.1137/18M1175768>.
22. A. Bernland, E. Wadbro, and M. Berggren, "Acoustic Shape Optimization Using Cut Finite Elements," *International Journal for Numerical Methods in Engineering* 113 (2018): 432–449.
23. E. Burman, S. Claus, P. Hansbo, M. G. Larson, and A. Massing, "CutFEM: Discretizing Geometry and Partial Differential Equations," *International Journal for Numerical Methods in Engineering* 104 (2015): 472–501.
24. P. Duysinx, L. Miegroet, T. Jacobs, and C. Fleury, "Generalized Shape Optimization Using X-FEM and Level Set Methods," in *IUTAM Symposium on Topological Design Optimization of Structures, Machines and Materials. Solid Mechanics and Its Applications*, vol. 137, ed. M. P. Bendsoe, N. Olhoff, and O. Sigmund (Springer Netherlands, 2006), 23–32.
25. E. Burman, D. Elfverson, P. Hansbo, M. G. Larson, and K. Larsson, "Shape Optimization Using the Cut Finite Element Method," *Computer Methods in Applied Mechanics and Engineering* 328 (2018): 242–261.
26. E. Bretin, J. Chapelat, P.-Y. Outtier, and Y. Renard, "Shape Optimization of a Linearly Elastic Rolling Structure Under Unilateral Contact Using Nitsche's Method and Cut Finite Elements," *Computational Mechanics* 70, no. 1 (2022): 205–224.
27. C. B. Dilgen and N. Aage, "Generalized Shape Optimization of Transient Vibroacoustic Problems Using Cut Elements," *International Journal for Numerical Methods in Engineering* 122, no. 6 (2021): 1578–1601.
28. S. B. Dilgen, J. S. Jensen, and N. Aage, "Shape Optimization of the Time-Harmonic Response of Vibroacoustic Devices Using Cut Elements," *Finite Elements in Analysis and Design* 196 (2021): 103608.
29. C. B. Dilgen and N. Aage, "Topology Optimization of Transient Vibroacoustic Problems for Broadband Filter Design Using Cut Elements," *Finite Elements in Analysis and Design* 234 (2024): 104123.
30. C. H. Villanueva and K. Maute, "CutFEM Topology Optimization of 3D Laminar Incompressible Flow Problems," *Computer Methods in Applied Mechanics and Engineering* 320 (2017): 444–473.
31. J. S. Dokken, A. Johansson, A. Massing, and S. W. Funke, "A Multimesh Finite Element Method for the Navier–Stokes Equations Based on Projection Methods," *Computer Methods in Applied Mechanics and Engineering* 368 (2020): 113129.

32. M. Berggren, "Shape Calculus for Fitted and Unfitted Discretizations: Domain Transformations vs. Boundary-Face Dilations," *Communications in Optimization Theory* 2023 (2023): 1–33.
33. Z. J. Wegert, J. Manyer, C. N. Mallon, S. Badia, and V. J. Challis, "Level-Set Topology Optimisation With Unfitted Finite Elements and Automatic Shape Differentiation," *Computer Methods in Applied Mechanics and Engineering* 445 (2025): 118203.
34. T.-P. Fries and T. Belytschko, "The Extended/Generalized Finite Element Method: An Overview of the Method and Its Applications," *International Journal for Numerical Methods in Engineering* 00 (2000): 1–6.
35. A. Sharma, H. Villanueva, and K. Maute, "On Shape Sensitivities With Heaviside-Enriched XFEM," *Structural and Multidisciplinary Optimization* 55, no. 2 (2017): 385–408.
36. E. Burman, "Ghost Penalty," *Comptes Rendus de L'académie Des Sciences - Series I - Mathematics* 348 (2010): 1217–1220.
37. F. Gibou, R. Fedkiw, and S. Osher, "A Review of Level-Set Methods and Some Recent Applications," *Journal of Computational Physics* 353 (2018): 82–109.
38. U. Naumann, *The Art of Differentiating Computer Programs* (Society for Industrial and Applied Mathematics, 2011).
39. M. Alnæs, J. Blechta, J. Hake, et al., "The FEniCS Project Version 1.5," *Archive of Numerical Software* 3, no. 100 (2015): 9–23.
40. M. C. Delfour and J.-P. Zolésio, *Shapes and Geometries. Metrics, Analysis, Differential Calculus, and Optimization*, 2nd ed. (SIAM, 2011).
41. J. Sokolowski and J.-P. Zolésio, *Introduction to Shape Optimization. Shape Sensitivity Analysis* (Springer-Verlag, 1992).
42. M. D. Delfour, "Topological Derivative: Semidifferential via Minkowski Content," *Journal of Convex Analysis* 25, no. 3 (2018): 957–982.
43. M. Berggren, "A Unified Discrete–Continuous Sensitivity Analysis Method for Shape Optimization," in *Applied and Numerical Partial Differential Equations. Computational Methods in Applied Sciences*, vol. 15, ed. W. Fitzgibbon, Y. A. Kuznetsov, P. Neittaanmäki, J. Periaux, and O. Pironneau (Springer, 2010).

Appendix A

Compression Driver Lumped-Parameter Model

We here provide a derivation of formula (4) under Assumptions 2.1. The geometry of the compression driver is characterized by its rest volume V_0 and the areas S_d , S_{wg} of its diaphragm and outlet. The easiest realization is the one of Figure 1, although much more general geometries are admissible due to the lumped-parameter nature of the model.

Imagine a stiff massless membrane of area S_{wg} positioned at the outlet of the chamber to the waveguide (the dashed tinted line in the cross-section view to the left in Figure 1). The velocity U_{wg} of this membrane will then be the same as the air velocity at the outlet. Under a movement of the diaphragm, the volume of the enclosed air between the piston and outlet membrane can be written as the sum of the rest volume V_0 plus an unsteady part V' ,

$$V(t) = V_0 + V'(t), \quad (\text{A1})$$

where the time derivative of the unsteady part satisfies

$$\dot{V}' = U_{wg}S_{wg} - U_dS_d, \quad (\text{A2})$$

in which U_d and U_{wg} are the velocities of the diaphragm and the massless membrane, respectively. The values $U_{wg}(t)$ and $U_d(t)$ are positive and negative, respectively, for velocities increasing the volume of the compression chamber.

By Assumption 2.1ii, the chamber will hold a uniform (but unsteady) pressure P , which satisfies, according to Assumption 2.1iii, the isentropy condition

$$PV^\gamma = \text{Const}, \quad (\text{A3})$$

where γ is the heat capacity ratio. Partitioning the pressure in the chamber into a steady and an unsteady part,

$$P(t) = p_0 + P'(t), \quad (\text{A4})$$

substituting expansions (A1) and (A4) into formula (A3), differentiating with respect to time, ignoring quadratic unsteady terms due to Assumption 2.1iv, and using expression (A2), we find that

$$\dot{P}' + \gamma \frac{p_0}{V_0} (U_{wg}S_{wg} - U_dS_d) = 0. \quad (\text{A5})$$

Using the fact that the speed of sound in an ideal gas (Assumption 2.1iii) satisfies

$$c_0^2 = \gamma \frac{p_0}{\rho_0}, \quad (\text{A6})$$

and definitions

$$d = \frac{V_0}{S_d}, \quad \kappa = \frac{S_d}{S_{wg}}, \quad (\text{A7})$$

where d is the depth of the chamber in the simple geometry of Figure 1 and κ the compression ratio, expression (A5) can be written

$$\dot{P}' + \frac{\rho_0 c_0^2}{d} \left(\frac{U_{wg}}{\kappa} - U_d \right) = 0. \quad (\text{A8})$$

Under time-harmonic excitation with frequency ω (Assumption 2.1i),

$$P'(t) = \text{Re}(pe^{i\omega t}), \quad U_{wg}(t) = \text{Re}(u_{wg}e^{i\omega t}), \quad U_d(t) = \text{Re}(u_d e^{i\omega t}), \quad (\text{A9})$$

expression (A8) becomes

$$i\omega p + \frac{\rho_0 c_0^2}{d\kappa} u_{wg} = \frac{\rho_0 c_0^2}{d} u_d = \frac{\rho_0 c_0^2}{d} \frac{1}{i\omega} a_d, \quad (\text{A10})$$

substituting velocity with acceleration amplitude a_d in the last equality. Due to the perfect termination of the waveguide (Assumption 2.1v), the acoustic pressure and velocity in the waveguide are proportional with proportionality constant the specific characteristic impedance $\rho_0 c_0$. Substituting $p = \rho_0 c_0 u_{wg}$ into Equation (A10) and multiplying with $i\omega d/c_0^2$, we find the requested formula

$$\left(-dk^2 + i \frac{k}{\kappa} \right) p = \rho_0 a_d, \quad (\text{A11})$$

where $k = \omega/c_0$ is the wave number.

Appendix B

Shape Calculus Details

Here we detail the calculations that yield expression (36), that is, the directional derivative of functional (29) with respect to the perturbation (30) of the level-set function.

Basic Formulas for Volume and Surface Integrals

The basic toolbox of shape calculus contains expressions of directional derivatives of integrals over a domain $\Omega \subset \mathbb{R}^d$ or its boundary $\partial\Omega$. The directional derivatives are defined with respect to *domain paths* $t \rightarrow \Omega_t$, where Ω_t is a family of domains parametrized by a scalar t in which $\Omega_0 = \Omega$. In the literature, such as in the classic monographs by Delfour & Zolésio [40] and Sokolowski & Zolésio [41], shape calculus is typically carried out assuming that the domain path is generated by a smooth homeomorphism $T_t : D \rightarrow \mathbb{R}^d$, where $D \subset \mathbb{R}^d$ is a *hold-all* containing all admissible domains. Thus, $\Omega_t = T_t(\Omega)$, and using a change of variables based on T_t , integrals over Ω_t and $\partial\Omega_t$ can be converted into integrals over Ω and $\partial\Omega$. The transformation parameters then appear explicitly in the integrands, which therefore can be differentiated using ordinary calculus. A particularly popular choice to generate the transformation is through a *perturbation of identity*, so that for any $\mathbf{x} \in \Omega$, $T_t(\mathbf{x}) = \mathbf{x} + t\mathbf{V}(\mathbf{x})$, where $\mathbf{V} : D \rightarrow \mathbb{R}^d$ is a vector field. The use of this type of transformation marries well with the need to modify a computational mesh to changes in the domain boundary. The so-called velocity field \mathbf{V} can then be used to displace the boundary mesh nodes as well as the internal nodes, the latter to preserve mesh quality.

The use of transformations to generate domain paths is less natural, however, in the current context. All admissible phase-plug shapes are confined within the hold-all D in Figure 6, but the computational mesh is fixed, the phase-plug wall is a boundary internal to D , and there are no transformations involved in the movement of the phase-plug wall. Nevertheless, from perturbation (30), a (nonunique) artificial velocity field \mathbf{V} can be defined locally on the mesh elements that are cut by the zero set of the level-set function (cf. Figure 7). The shape calculus carried out in our previous work using a 2D CutFEM approach [21, 22] relied on such an approach.

However, it is not necessary to invoke transformations and artificial velocity fields in this case. An alternative is to generalize a method introduced by Delfour [42] and consider *dilations*, generated by perturbation (30), of surface patches defined by the level-set function. We will here rely on formulas for the shape derivative of domain and boundary integrals as derived, using such a method, in a recent contribution by the first author [32]. These formulas assume minimal smoothness and take into account that the design boundary will contain edges and a discontinuous normal field when the design boundary intersects mesh surfaces, as illustrated in Figure 8. The presence of such discontinuities did not affect the shape calculus in our previous work, due to the natural boundary condition assumed there. Here, however, the viscothermal boundary terms in the bilinear form (10a) contain discontinuities that need to be handled.

We thus consider a continuous, piecewise-linear level-set function ϕ_h , defined on a fixed triangulation \mathcal{T}_h on D , generating the computational domain Ω_h , defined by the condition $\phi_h < 0$. Consider then a perturbation.

$$\phi_{h,t} = \phi_h + t w, \quad (\text{B1})$$

where w is a Lagrangian basis function and $t \in \mathbb{R}$. This perturbation generates perturbed domains: $\Omega_{h,t} \subset \Omega_h$ when $t > 0$ and $\Omega_{h,t} \supset \Omega_h$ when $t < 0$; the inclusions are due to the fact that each basis function w for continuous, piecewise-linear functions satisfies $w \geq 0$. The following formula for the shape derivative of volume integrals over Ω_h holds.

Theorem B.1. *Under perturbation (B1) and for $t \mapsto f(t)$ and $t \mapsto f'(t)$ continuous in some nonempty interval $[0, t_{\max}]$ such that $f(t), f'(t) \in C^0(\overline{\mathcal{T}_h})$ on $(0, t_{\max})$, the directional semiderivative of volume integral*

$$J_1(\phi_{h,t}) = \int_{\Omega_{h,t}} f_t \, dV \tag{B2}$$

at $t = 0$ satisfies

$$dJ_1(\phi_h; w) = \lim_{t \rightarrow 0^+} \frac{1}{t} (J_1(\phi_{h,t}) - J_1(\phi_h)) = \int_{\Omega_h} f' \, dV - \int_{\partial\Omega_h} f \frac{w}{|\partial_n \phi_h|} \, dS. \tag{B3}$$

Remark B.2. The notation $g \in C^k(\overline{\mathcal{T}_h})$ means that $g|_K \in C^k(\overline{K})$ for each element $K \in \mathcal{T}_h$.

Theorem B.1 is an immediate consequence of the same theorem proven for a fixed $f \in C^0(\overline{\mathcal{T}_h})$ ([32], Theorem 6.7), for which the first term on the right side in expression (B3) vanishes. The full formula follows from the product rule of differentiation under the assumptions on $t \mapsto f(t)$ given above. Note that the theorem only refers to a one-sided derivative; the limits $t \rightarrow 0^+$ and $t \rightarrow 0^-$ both exist but may be different. (The proof for the two cases is entirely analogous.) The reason for this lack of strong differentiability is that f as well as $\partial_n \phi_h$ are allowed to contain jump discontinuities across mesh faces. These discontinuities become an issue for domains like the one to the left in Figure B1, where $\int_{S \cap \partial\Omega} dS > 0$ for some mesh face S . For basis functions w associated with the end points of such an S , Formula (B3) holds for the limit of f and $\partial_n \phi_h$ on S from the interior of Ω_h ; (Recall that $\Omega_{h,t} \subset \Omega_h$ for $t \geq 0$.) When the limit $t \rightarrow 0^-$ is considered, it will be the limit of the values from the exterior that should be employed, since $\Omega_{h,t} \supset \Omega_h$ for $t \leq 0$. However, when $\partial\Omega_h$ only cuts through the interior of the mesh elements, as in the right picture of Figure B1, the limits as $t \rightarrow 0^+$ and $t \rightarrow 0^-$ will agree, since then f and $\partial_n \phi_h$ will vary continuously under small enough perturbations of the boundary.

To carry out the shape calculus, we will need, in addition to formula (B3), also the corresponding formula for integrals over $\partial\Omega_h$. Note that any nonempty boundary segment $\partial\Omega_h \cap K$, for some tetrahedral element $K \in \mathcal{T}_h$, will either be a triangle or a quadrilateral. At the edges of each such $\partial\Omega_h \cap K$, we will need to use the concept of conormals, introduced in Section 7. These will be used to define limits and jumps of functions across line segments $\partial\Omega_h \cap S$, where S is a mesh face, as illustrated in Figure 8.

The following theorem is an immediate consequence of the same theorem proven for a fixed $f \in C^1(\overline{\mathcal{T}_h})$ ([32], Theorem 6.11). Similarly to Theorem B.1, nondifferentiability can be expected when some mesh face S aligns with $\partial\Omega_h$, like in the domain to the left in Figure B1. However, the ambiguities due to the discontinuities in the integrand of the last term in the expression for dJ_2 below are not as easily resolved as in Theorem B.1. Thus, the proof of Theorem B.3 ([32], Theorem 6.11) is restricted to domains where the boundary does not intersect any mesh nodes, such as the one to the right in Figure B1.

Theorem B.3. *Assume that the boundary $\partial\Omega_h$ of the domain Ω_h does not intersect with any mesh nodes. Then, under perturbation (B1) and for $t \mapsto f(t)$ and $t \mapsto f'(t)$ being continuous in some nonempty interval $[0, t_{\max}]$ such that $f(t), f'(t) \in C^1(\overline{\mathcal{T}_h})$ on $(0, t_{\max})$, the directional*

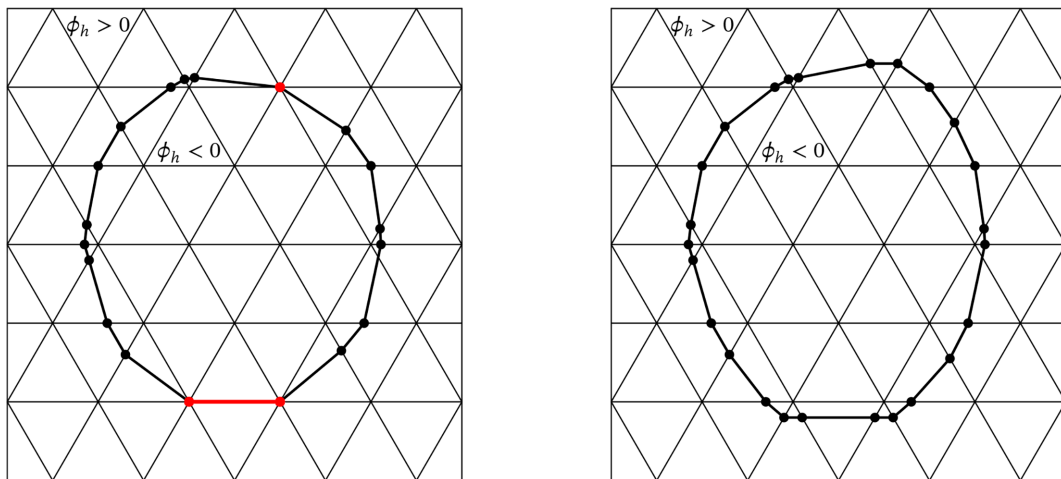


FIGURE B1 | Examples in 2D of a meshed rectangular hold-all D and domains Ω_h generated by level-set functions ϕ_h defined on the mesh in the figure. Both types of domains are admissible for Theorem B.1, although only one-sided derivatives exist for domains like the one to the left, where a mesh face is contained in the boundary. However, the proof ([32], Theorem 6.11) of Theorem B.3 requires domains like the one to the right, where the domain boundary does not intersect any mesh nodes.

derivative of surface integral

$$J_2(\phi_{h,t}) = \int_{\partial\Omega_{h,t}} f_t \, dS \tag{B4}$$

at $t = 0$ satisfies

$$dJ_2(\phi_h, w) = \int_{\partial\Omega_h} \left(f' - \frac{\partial f}{\partial n} \frac{w}{|\partial_n \phi_h|} \right) dS - \sum_{S \in \mathcal{S}_h} \int_{\partial\Omega_h \cap S} \mathbf{n}^S \cdot \llbracket f \mathbf{m} \rrbracket \frac{w}{|\partial_{n^S} \phi_h|} d\gamma, \tag{B5}$$

where \mathbf{n}^S is the normal vector to $\partial\Omega_h \cap S$, located in S and outward-directed from Ω_h , and where $\llbracket f \mathbf{m} \rrbracket = f_1 \mathbf{m}_1 + f_2 \mathbf{m}_2$. Here, for $k = 1, 2$, \mathbf{m}_k are the conormals to $\partial\Omega \cap K_k$ at $\partial\Omega \cap S$, where $K_1, K_2 \in \mathcal{T}_h$ such that $\bar{S} = \bar{K}_1 \cap \bar{K}_2$. Each \mathbf{m}_k lies in the plane of and is directed outward from $\partial\Omega_h \cap K_k$, and f_k is the limit f on S defined by $f_k(\mathbf{x}) = \lim_{\epsilon \rightarrow 0^+} f(\mathbf{x} - \epsilon \mathbf{m}_k)$, for any $\mathbf{x} \in S$.

It is illuminating to compare directional derivatives (B3) and (B5) with the traditional expressions, that is, the formulas obtained when utilizing domain transformations through a perturbation of identity. For domain integrals, the classical formula is

$$J_1(\Omega; \mathbf{V}) = \int_{\Omega} f' \, dV + \int_{\partial\Omega} f \mathbf{V} \cdot \mathbf{n} \, dS \tag{B6}$$

The proof by Delfour & Zolésio ([40], Ch. 9, Theorem 4.2) holds for Lipschitz domains Ω , velocity fields satisfying $\mathbf{V} \in C^1(D)^d$ and for functions $t \mapsto f_t$ continuous with values in $W^{1,1}(D)$ and differentiable with values in $L^1(D)$. For the boundary integral, the classical formula is

$$J_2(\Omega; \mathbf{V}) = \int_{\partial\Omega} f' \, dS + \int_{\partial\Omega} \left(\frac{\partial f}{\partial n} + \kappa f \right) \mathbf{V} \cdot \mathbf{n} \, dS, \tag{B7}$$

where κ is the local summed curvature (twice the mean curvature) of the boundary. The conditions for the boundary integral formula are quite restrictive. The proof by Delfour & Zolésio ([40], Ch. 9, Theorem 4.2) holds for Ω of class C^2 and for continuous functions $t \mapsto f_t$ with values in $H^2(D)$.

Comparing our formulas (B3) and (B5) with the classical (B6) and (B7), we first note that the term $-w/|\partial_n \phi_h|$ corresponds to the normal velocity $\mathbf{V} \cdot \mathbf{n}$ in the classical formulas. Secondly, we note that the last integral in expression (B5) is a discrete counterpart to the curvature term in expression (B7). Note that the requirement for formula (B7) of a C^2 -regular domain and an integrand $f \in H^2(D)$ is violated in our case.

Calculation of Directional Derivative (36)

Based on the basic formulas of theorems (B.1) and (B.3), we here provide the details of the calculation of directional derivative (36). Due to the differentiability subtleties associated with Theorem B.3, we will, for the calculations below, assume that the boundary $\partial\Omega_h$ does not intersect any mesh nodes, as in the domain on the right in Figure B1.

We will follow a standard approach, in which the objective function (29) is treated as the composite mapping $\phi_h \mapsto p_h \mapsto j$. Differentiation of this mapping yields the shape derivative p'_h as an intermediate quantity. As we do not prove the existence of p'_h , the derivation will be formal. However, if p'_h exists, it is necessarily of the same regularity as p_h , since it is only the coefficients in an expansion in a finite-element basis that will be differentiated due to our use of a fixed computational mesh. Note that the situation is very different for shape calculus in the context of body-fitted and deforming meshes, as discussed in detail in previous publications [32, 43]. Then the use of the product rule on the expansion of p_h requires differentiation also of the basis functions, since their support will be perturbed. As a consequence, it turns out that the shape derivative p'_h will then contain jump discontinuities. Therefore, for deforming meshes, the shape calculus cannot be carried out as below, and the final expression will then depend also on interior values of the state and adjoint states, not only on boundary quantities like in expression (36) [32, 43].

Recall from Section 6 that the solution space W_h to problem (23) will not be fixed throughout the optimization, since it is spanned by the basis functions whose support intersect domain Ω_h with positive measure. As illustrated in Figure 7, the nodal degrees of freedom for W_h , marked black in the figure, are located not just inside Ω_h but also outside the domain for the elements whose interior intersects the boundary. Considering now perturbation (30) for nonzero t , we note the nodal degrees of freedom for W_h only change when the domain boundary moves away from an intersection with a mesh node. Thus, under the assumption made above—that the boundary $\partial\Omega_h$ does not intersect any mesh node—we conclude that when starting with t sufficiently small, W_h will not change during the limit process $t \rightarrow 0$.

Thus, given the solution space W_h , there is a $t_{\max} > 0$ such that for each $t \in [0, t_{\max}]$, the discrete acoustic pressure on the perturbed domain will satisfy the following problem.

$$\begin{aligned} &\text{Find } p'_h \in W_h \text{ such that } \forall q_h \in W_h, \\ &\int_{\Omega'_h} \nabla q_h \cdot \nabla p'_h - k^2 \int_{\Omega'_h} q_h p'_h + \text{ik} \int_{\Gamma_{\text{out}}} q_h p'_h + \int_{\Gamma'_{w,h}} \psi(q_h, p'_h; \mathbf{n}') + \epsilon_h s_h(q_h, p'_h) = \int_{\Gamma_d} \rho_0 q_h a_d \mathbf{n} \cdot \mathbf{e}_a. \end{aligned} \tag{B8}$$

where ψ is defined in expression (33). Consequently, the average acoustic pressure at the outlet becomes

$$j(\phi'_h) = \frac{1}{|\Gamma_{\text{out}}|} \int_{\Gamma_{\text{out}}} p'_h. \quad (\text{B9})$$

Note that the outlet boundary Γ_{out} is unchanged by the perturbation. The *shape derivative* of p'_h at $t = 0$, defined by

$$p'_h = \lim_{t \rightarrow 0} \frac{1}{t} (p'_h - p_h^0), \quad (\text{B10})$$

is also an element in \mathcal{W}_h , since $p'_h \in \mathcal{W}_h$ for each $t \in [0, t_{\text{max}}]$. Differentiating objective function (B9) at $t = 0$ yields

$$dj(\phi_h; w_l) = \int_{\Gamma_{\text{out}}} p'_h. \quad (\text{B11})$$

To determine an explicit expressions for directional derivative dj in terms of w_l , we start by differentiating Equation (B8) at $t = 0$, utilizing formulas (B3) and (B5), to find that, for each $q_h \in \mathcal{W}_h$,

$$\begin{aligned} & \int_{\Omega_h} \nabla q_h \cdot \nabla p'_h - k^2 \int_{\Omega_h} q_h p'_h - \int_{\partial\Omega_h} (\nabla q_h \cdot \nabla p_h - k^2 q_h p_h) \frac{w_l}{|\partial_n \phi_h|} + ik \int_{\Gamma_{\text{out}}} q_h p'_h \\ & + \int_{\Gamma_{w,h}} \psi'(q_h, p_h; \mathbf{n}) - \int_{\Gamma_{w,h}} \frac{\partial}{\partial n} \psi(q_h, p_h; \mathbf{n}) \frac{w_l}{|\partial_n \phi_h|} - \sum_{S \in \mathcal{S}_h} \int_{\Gamma_{w,h} \cap S} \mathbf{n}^S \cdot \llbracket \psi(q_h, p_h; \mathbf{n}) \mathbf{m} \rrbracket \frac{w_l}{|\partial_{n^S} \phi_h|} \\ & + \epsilon_h s_h(q_h, p'_h) = 0. \end{aligned} \quad (\text{B12})$$

Here, similarly as previously observed in the analogous 2D case [21], we have used the fact that the mapping $t \mapsto s_h(q_h, p'_h)$ is differentiable, which is a consequence of our assumption that the boundary $\partial\Omega'_h$ does not intersect any mesh node. Differentiating ψ , using definition (33), we find that

$$\begin{aligned} \psi'(q_h, p_h; \mathbf{n}) &= \frac{d}{dt} \psi(q_h, p'_h; \mathbf{n}^t) \Big|_{t=0} \\ &= \alpha_T q_h p'_h + \alpha_V \left(\nabla q_h \cdot \nabla p'_h - \mathbf{n}' \cdot \nabla q_h \frac{\partial p_h}{\partial n} - \frac{\partial q_h}{\partial n} \mathbf{n}' \cdot \nabla p_h - \frac{\partial q_h}{\partial n} \frac{\partial p'_h}{\partial n} \right) \\ &= \alpha_T q_h p'_h + \alpha_V \nabla_{\top} q_h \cdot \nabla_{\top} p'_h - \alpha_V \left(\mathbf{n}' \cdot \nabla q_h \frac{\partial p_h}{\partial n} + \frac{\partial q_h}{\partial n} \mathbf{n}' \cdot \nabla p_h \right), \end{aligned} \quad (\text{B13})$$

where

$$\alpha_T = \delta_T k^2 \frac{(i-1)(\gamma-1)}{2}, \quad \alpha_V = \delta_V \frac{i-1}{2}. \quad (\text{B14})$$

Notice that \mathbf{n}' vanishes everywhere except on the part of the phase-plug boundary affected by the perturbation, $\Gamma_{p,h}$, on which the perturbed normal field satisfies

$$\mathbf{n}' = \frac{\nabla(\phi_h + tw_l)}{|\nabla(\phi_h + tw_l)|} \quad \text{on } \Gamma'_{p,h}. \quad (\text{B15})$$

We will differentiate the right side of the expression (B15), starting with the denominator

$$\begin{aligned} \frac{d}{dt} \left| \nabla(\phi_h + tw_l) \right| \Big|_{t=0} &= \frac{d}{dt} \left(\nabla(\phi_h + tw_l) \cdot \nabla(\phi_h + tw_l) \right)^{1/2} \Big|_{t=0} \\ &= \left(\nabla(\phi_h + tw_l) \cdot \nabla(\phi_h + tw_l) \right)^{-1/2} \nabla(\phi_h + tw_l) \cdot \nabla w_l \Big|_{t=0} \\ &= \frac{\nabla \phi_h \cdot \nabla w_l}{|\nabla \phi_h|}, \end{aligned} \quad (\text{B16})$$

from which it follows that

$$\frac{d}{dt} \left| \nabla(\phi_h + tw_l) \right| \Big|_{t=0} = \frac{|\nabla \phi_h| \nabla w_l - \nabla \phi_h \frac{\nabla \phi_h \cdot \nabla w_l}{|\nabla \phi_h|}}{|\nabla \phi_h|^2} = \left(1 - \frac{\nabla \phi_h}{|\nabla \phi_h|} \otimes \frac{\nabla \phi_h}{|\nabla \phi_h|} \right) \frac{\nabla w_l}{|\nabla \phi_h|}. \quad (\text{B17})$$

From expressions (B15) and (B17) and the fact that $\nabla \phi_h \Big|_{\Gamma_{p,h}} = \mathbf{n} \partial_n \phi_h \Big|_{\Gamma_{p,h}}$ almost everywhere on $\Gamma_{p,h}$ follows that

$$\mathbf{n}' = \frac{P_{\top} \nabla w_l}{|\partial_n \phi_h|} \quad \text{a. e. on } \Gamma_{p,h}, \quad (\text{B18})$$

where

$$P_T = I - \mathbf{n} \otimes \mathbf{n} \tag{B19}$$

is the projector on the tangent plane of $\Gamma_{p,h}$. Substituting expression (B18) into formula (B13), we find that

$$\psi'(q_h, p_h; \mathbf{n}) = \begin{cases} \psi(q_h, p'_h; \mathbf{n}) & \text{on } \Gamma_{w,h} \setminus \Gamma_{p,h} \\ \psi(q_h, p'_h; \mathbf{n}) - \alpha_V \left(\frac{(P_T \nabla w_l) \cdot \nabla q_h}{|\partial_n \phi_h|} \frac{\partial p_h}{\partial n} + \frac{\partial q_h}{\partial n} \frac{(P_T \nabla w_l) \cdot \nabla p_h}{|\partial_n \phi_h|} \right) & \text{on } \Gamma_{p,h}, \end{cases} \tag{B20}$$

which, substituted in expression (B12), yields that $\forall q_h \in W_h$,

$$\begin{aligned} & \int_{\Omega_h} \nabla q_h \cdot \nabla p'_h - k^2 \int_{\Omega_h} q_h p'_h - \int_{\Gamma_{p,h}} (\nabla q_h \cdot \nabla p_h - k^2 q_h p_h) \frac{w_l}{|\partial_n \phi_h|} + ik \int_{\Gamma_{out}} q_h p'_h \\ & + \int_{\Gamma_{w,h}} \psi(q_h, p'_h; \mathbf{n}) - \alpha_V \int_{\Gamma_{p,h}} \left(\frac{(P_T \nabla w_l) \cdot \nabla q_h}{|\partial_n \phi_h|} \frac{\partial p_h}{\partial n} + \frac{\partial q_h}{\partial n} \frac{(P_T \nabla w_l) \cdot \nabla p_h}{|\partial_n \phi_h|} \right) \\ & - \int_{\Gamma_{p,h}} \frac{\partial}{\partial n} \psi(q_h, p_h; \mathbf{n}) \frac{w_l}{|\partial_n \phi_h|} - \sum_{S \in \mathcal{S}_h} \int_{\Gamma_{p,h} \cap S} \mathbf{n}^S \cdot \llbracket \psi(q_h, p_h; \mathbf{n}) \mathbf{m} \rrbracket \frac{w_l}{|\partial_n \phi_h|} + \epsilon_h s_h(q_h, p'_h) = 0, \end{aligned} \tag{B21}$$

where we, for integral terms 3, 7 and 8, also have used that w_l vanishes on $\partial\Omega_h \setminus \Gamma_{p,h}$.

Now let $z_h \in W_h$ satisfy the adjoint equation

$$\int_{\Omega_h} \nabla w_h \cdot \nabla z_h - k^2 \int_{\Omega_h} w_h z_h + ik \int_{\Gamma_{out}} w_h z_h + \int_{\Gamma_{w,h}} \psi(w_h, z_h; \mathbf{n}) + \epsilon_h s_h(w_h, z_h) = \int_{\Gamma_{out}} w_h \quad \forall w_h \in W_h. \tag{B22}$$

In particular, evaluating the adjoint equation for $w_h = p'_h$ yields that

$$\int_{\Omega_h} \nabla p'_h \cdot \nabla z_h - k^2 \int_{\Omega_h} p'_h z_h + ik \int_{\Gamma_{out}} p'_h z_h + \int_{\Gamma_{w,h}} \psi(p'_h, z_h; \mathbf{n}) + \epsilon_h s_h(p'_h, z_h) = \int_{\Gamma_{out}} p'_h. \tag{B23}$$

Substituting expression (B23) into expression (B21) with $q_h = z_h$, the resulting expression reduces to

$$\begin{aligned} & \int_{\Gamma_{out}} p'_h - \int_{\Gamma_{p,h}} (\nabla z_h \cdot \nabla p_h - k^2 z_h p_h) \frac{w_l}{|\partial_n \phi_h|} - \alpha_V \int_{\Gamma_{p,h}} \left(\frac{(P_T \nabla w_l) \cdot \nabla z_h}{|\partial_n \phi_h|} \frac{\partial p_h}{\partial n} + \frac{\partial z_h}{\partial n} \frac{(P_T \nabla w_l) \cdot \nabla p_h}{|\partial_n \phi_h|} \right) \\ & - \int_{\Gamma_{p,h}} \frac{\partial}{\partial n} \psi(z_h, p_h; \mathbf{n}) \frac{w_l}{|\partial_n \phi_h|} - \sum_{S \in \mathcal{S}_h} \int_{\Gamma_{p,h} \cap S} \mathbf{n}^S \cdot \llbracket \psi(z_h, p_h; \mathbf{n}) \mathbf{m} \rrbracket \frac{w_l}{|\partial_n \phi_h|} = 0, \end{aligned} \tag{B24}$$

where we also have used that s_h is symmetric and ψ is symmetric in its first two arguments.

Finally, from expressions (B11) and (B24) we obtain the directional derivative expression

$$\begin{aligned} dj(\phi_h; w_l) &= \int_{\Gamma_{p,h}} (\nabla z_h \cdot \nabla p_h - k^2 z_h p_h) \frac{w_l}{|\partial_n \phi_h|} \\ & + \alpha_V \int_{\Gamma_{p,h}} \left(\frac{(P_T \nabla w_l) \cdot \nabla z_h}{|\partial_n \phi_h|} \frac{\partial p_h}{\partial n} + \frac{\partial z_h}{\partial n} \frac{(P_T \nabla w_l) \cdot \nabla p_h}{|\partial_n \phi_h|} \right) \\ & + \int_{\Gamma_{p,h}} \frac{\partial}{\partial n} \psi(z_h, p_h; \mathbf{n}) \frac{w_l}{|\partial_n \phi_h|} + \sum_{S \in \mathcal{S}_h} \int_{\Gamma_{p,h} \cap S} \mathbf{n}^S \cdot \llbracket \psi(z_h, p_h; \mathbf{n}) \mathbf{m} \rrbracket \frac{w_l}{|\partial_n \phi_h|}, \end{aligned} \tag{B25}$$

under perturbation (30), where p_h solves state Equation (B8) for $t = 0$ and z_h adjoint Equation (B22).